Prognostic Value of Optimized Dynamic Contrast-Enhanced Magnetic Resonance Imaging of High-Grade Gliomas

Christopher Larsson

Doctoral Thesis

2018

Faculty of Medicine
University of Oslo

The Intervention Centre
and
Department of Diagnostic Physics

Oslo University Hospital
Norway

© Christopher Larsson, 2018

Series of dissertations submitted to the
Faculty of Medicine, University of Oslo

ISBN 978-82-8377-259-3

All rights reserved. No part of this publication may be
reproduced or transmitted, in any form or by any means, without permission.

Cover: Hanne Baadsgaard Utigard.
Print production: Reprosentralen, University of Oslo.

Acknowledgments

This thesis was performed at the Intervention Centre at Oslo University Hospital Rikshospitalet and the Department of Diagnostic Physics as part of a high-grade glioma monitoration study between 2010 and 2017.

This thesis could not have been completed without the contribution of several people;

First, I would like to thank Inge Groote and Atle Bjørnerud; my supervisors and founders of the project. This work could not have been done without your help and support. I started out as a medical student without any idea of what I had signed up for and I will forever be grateful for your guidance and patience trough my slow metamorphosis into a (hopefully) full grown researcher.

A sincere thanks to the Intervention Centre, Rikshospitalet with my co-supervisor Professor Erik Fosse for letting me do my research there, and have access to a 3 Tesla scanner free from the busy schedule of a clinical magnet. I would also like to thank the Department of Diagnostic Physics and Anne Catrine Martinsen for giving me space to finish this thesis after several years as a nomad in search of office space wandering the halls of Rikshospitalet.

My nearest collaborator on the first two papers Magne Kleppestø started in the research group at the same time as me. Our partnership on this project has been a constant source of delight and our different backgrounds an invaluable part of our cooperation. I look forward to further collaborations in the future and the finish of your own thesis.

Jonas Vardal, a fellow medical student when we began this journey; thanks for climbing the steep mountain learning MRI at the same time as me. Your help in handling of the

patients has been invaluable to the project. To Raimo Salo and Tuva Hope for the nice coffee talks and insight in data management.

A big thanks to Grethe Løvland, Terje Tillung and Svein Are Vatnehol who must be among the most patient and flexible radiographers out there. To Paulina Due Tønnesen who was an integrated part of developing this study and did all the neuro-radiological assessment of all patients, Petter Brandal, MD, PhD, for recruitment and valuable insight on patients with gliomas and their development. I would also like to thank all other co-authors for their contribution on each paper.

To my family and friends whom I haven't seen half as often as I have wanted in the last years. I hope I can make up for the time lost in the future. To my most beloved Josephine, whom I stumbled upon in the middle of the writing of the last paper and the thesis. Neither of us knew what we were in for and I would not change any minute of our time together. You have been patient beyond words, supporting me all the way.

And lastly but most importantly, to all the patients who agreed to be a part of this study; I sincerely hope our research will contribute to more knowledge and better therapy for glioma patients in the future.

Table of contents

Acknowledgments III
Table of contents V
Abbreviations 1
List of papers 3
1 Introduction 5
1.1 Gliomas 6
1.1.1 Grading and classification of gliomas 6
1.1.2 Treatment of high-grade gliomas 10
1.2 Magnetic resonance imaging 13
1.2.1 Basics of magnetic resonance imaging 13
1.2.2 Contrast agents in magnetic resonance imaging 16
1.2.3 Perfusion-weighted magnetic resonance imaging 18
1.3 Magnetic resonance imaging of gliomas 29
1.3.1 Structural magnetic resonance imaging in gliomas 29
1.3.2 Response criteria in high-grade gliomas 30
1.3.3 Imaging of radiation-induced injury and pseudoprogression 32
1.3.4 Perfusion magnetic resonance imaging in gliomas 33
1.4 Prognostics in gliomas 35
1.5 Summary of introduction 39
2 Aim of this thesis 43
3 Material and methods 45
3.1 Overall design 45
3.2 Ethical statement: 45
3.3 Imaging protocol 45
3.4 Computer simulations 46
3.5 Data analysis 47
3.5.1 Image co-registration 47
3.5.2 Region-of-Interest generation 48
3.5.3 Downsampling and truncation 49
3.5.4 Arterial input generation 51
3.5.5 Dynamic contrast-enhanced magnetic resonance imaging analysis 52
3.5.6 Dynamic susceptibility contrast magnetic resonance imaging analysis 52
4 Summary of papers 55
5 Discussion 59

5.1 Temporal resolution and total acquisition time 59
5.2 T_1 mapping 61
5.3 Issues with prognostic imaging markers 63
6 Conclusion and future perspectives 67
6.1 Conclusion 67
6.2 Future perspectives 68
7 Errata 69
8 References 71
Papers I-III 89

Abbreviations

AIF	Arterial input function
ASL	Arterial spin labeling
BBB	Blood-brain barrier
CA	Contrast agent
CE	Contrast enhancement
CBF	Cerebral blood flow
CBV	Cerebral blood volume
CT	Computer tomography
DCE	Dynamic contrast-enhanced
DSC	Dynamic susceptibility contrast
DWI	Diffusion-weighted imaging
EES	Extravascular extracellular space
EPI	Echo-planar imaging
FLAIR	Fluid-attenuated inversion recovery
GBCA	Gadolinium-based contrast agent
Gd	Gadolinium
GBM	Glioblastoma
HGG	High-grade glioma
IDH	Isocitrate dehydrogenase
LGG	Low-grade glioma
k_{ep}	Rate constant for contrast agent reflux from EES to plasma space
KPS	Karnofsky Performance Score
K^{trans}	Contrast agent transfer constant from the plasma space to EES
MGMT	O^6-methylguanin-DNA methyl transferase
MRI	Magnetic resonance imaging
NMR	Nuclear Magnetic Resonance

NOS	Not otherwise specified
OS	Overall survival
PFS	Progression-free survival
pMRI	Perfusion MRI
PS	Permeability surface area product
QIBA	Quantitative Imaging Biomarker Alliance
RANO	Response Assessment in Neuro-Oncology Working Group
r	Relative
RECIST	Response Evaluation Criteria in Solid Tumors
RF	Radio frequency
RT	Radiation therapy
ROI	Region-of-interest
SNR	Signal-to-noise ratio
T1w	T1-weighted
$T_1(0)$	Baseline T_1
T2w	T2-weighted
T_{acq}	Total acquisition time
TMZ	Temozolomide
T_s	Temporal resolution
v_e	Fractional EES
v_p	Fractional tissue plasma volume
WHO	World Health Organization

List of papers

Paper I:

Sampling Requirements in DCE-MRI Based Analysis of High Grade Gliomas: Simulations and Clinical Results.

Larsson C, Kleppestø M, Rasmussen I, Salo R, Vardal J, Brandal P, Bjørnerud A.

J Magn Reson Imaging 2013;37:818-829.

Paper II:

T_1 in High Grade Glioma and the Influence of Different Measurement Strategies on Parameter Estimations in DCE-MRI.

Larsson C, Kleppestø M, Groote IR, Vardal J, Bjørnerud A.

J Magn Reson Imaging 2015;42:97-104.

Paper III:

Prediction of Survival and Progression in Glioblastoma Patients using Temporal Perfusion Changes during Radiochemotherapy.

Larsson C, Groote IR, Vardal J, Kleppestø M, Odland A, Brandal P, Due-Tønnessen P, Holme SS, Hope TR, Meling TR, Emblem KE, Bjørnerud A.

(Submitted)

1 Introduction

Gliomas are the most common primary brain tumors and originate from the glial cells in the brain[1]. Initial diagnosis is often made using magnetic resonance imaging (MRI), which enables rough differential diagnosis from other conditions. Despite advances in surgery, radiotherapy (RT) and chemotherapy, the median survival of glioblastomas (GBMs), the most malignant gliomas, is around one year[2]. However, some subgroups of patients survive far longer than this, despite being given the same standardized treatment. Although specific genetic biomarkers in surgical biopsy material are associated with a better than average prognosis[3], no established imaging biomarkers exists to stratify patients with a better than average overall survival (OS) during treatment.

Treatment response is assessed by changes in tumor volume on MRI. However, increase in tumor volume during the first months after RT can be caused by both recurrent disease and treatment related changes[4], two entities similar in appearance but with large differences in OS. More advanced MRI methods are thus investigated to more accurately reflect the pathologic heterogeneity of gliomas and for better prediction of survival[5].

Perfusion MRI (pMRI) are advanced MRI methods measuring the integrity of the blood vessel, the cerebral blood flow (CBF) and the cerebral blood volume (CBV). The use of pMRI has shown promise for glioma grading and early prognostics[5]. It is, however, recognized that a lack of standardization of the advanced MRI methods is a main hindrance for widespread clinical use and comparison of results between studies. In addition, the timing of imaging varies greatly between studies, further complicating

comparison. An optimization and standardization of the pMRI sequences, timing of imaging and analysis approach are warranted, hopefully leading to more accurate and similar prediction of OS between cancer centers. Furthermore, better OS prediction will help find candidates suitable for aggressive treatment at an early stage. Alternatively, patients that will not benefit significantly from therapy could be spared from the severe burden of receiving it in the last phase of their lives.

1.1 Gliomas

Gliomas are a subtype of the primary brain tumors from the glial cells in the brain and consists of 30 % of all primary brain tumors and 80 % of all malignant brain tumors[1]. Common symptoms of a brain tumor are headache, epileptic seizures, personality changes and cognitive decline. A fast onset of symptoms may reflect rapid tumor growth and increased severity of the disease. Gliomas are derived from astrocytic, ependydemal or oligodendrial cells with astrocytic tumors accounting for two thirds of all gliomas[6]. A considerable intra- and intergroup heterogeneity in gliomas exist[7]. They can be divided in high-grade glioma (HGG) and low-grade glioma (LGG). HGGs are by far the most frequent, accounting for around 80 % of all gliomas, and deadly[8,9]. Incidence has been steadily rising over the last 50 years with around 200 new cases of HGG diagnosed in Norway annually[10].

1.1.1 Grading and classification of gliomas

Glioma grading was introduced in 1926 by the famous neurosurgeon Harvey Cushing (1869-1939). The classification of gliomas was based fully upon the similarities between the normal glia cells and presumed levels of differentiation as observed using the light

microscope. Molecular parameters were added to the histopathological features in the recent updated World Health Organization (WHO) classification of tumors of the central nervous system[11]. The WHO grading system recognizes four stages, with increasing stage index signifying increasingly aggressive tumor behavior, shorter survival, and more rapid disease progression. WHO grade I and II are collectively known as LGG while HGG includes grade III-IV. HGGs are also known as malignant gliomas. Of the grade IV gliomas GBM is the most common type and the name GBM will hereafter be used for grade IV tumors. GBMs are further divided in primary or secondary[8]. Primary GBMs are lesions without clinical signs of a precursor lesion and secondary GBMs are derived from grade II or grade III gliomas[12]. A flowchart of the classification of the most common gliomas is shown in figure 1.

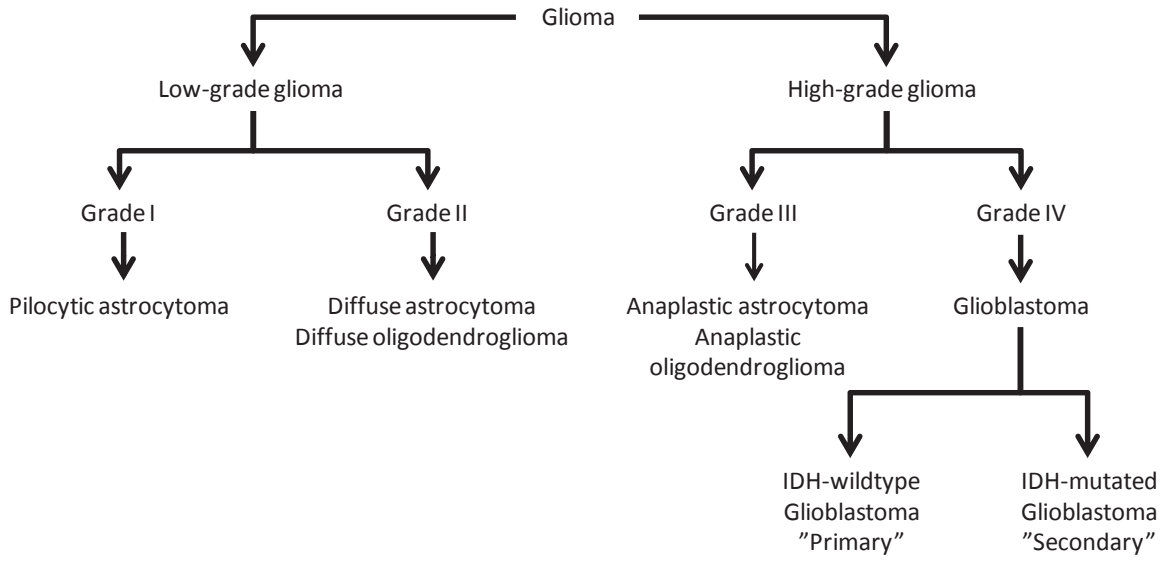

Figure 1. Flowchart of the most common gliomas in a hierarchical manor. The new classification of gliomas using molecular markers is only shown for GBMs.

Histopathologic features of gliomas

The histopathological features of grade II gliomas are typically well-differentiated tumors without signs of anaplasia. A higher degree of nuclear pleomorphy, increased mitotic activity and increased cellularity is characteristic for both grade III gliomas and GBMs. Signs of necrosis are pathognomonic of GBM, and a characteristic proliferated microvasculature is seen around the necrosis exhibiting a glomerulus- or garland-like appearance. Histological differentiation of primary and secondary GBM is almost impossible[12]. Typical histopathological findings in some common glioma subtypes are shown in figure 2.

Molecular markers

The most important molecular parameter in the classification of gliomas is mutations in the gene coding for the enzyme isocitrate dehydrogenase (IDH)[11,13]. Most gliomas are now specified as either IDH-mutant, IDH-wildtype (i.e. no mutation of IDH) or "not otherwise specified" (NOS)[11]. IDH-mutations are found in 80% of grade II and III gliomas and secondary GBMs, with a much lower percentage in primary GBMs. About 90 % of all GBMs are IDH-wildtype and clinically defined as primary GBMs. IDH-wildtype GBMs are predominantly found in patients older than 55 years of age[11,12]. IDH-mutant GBMs are typically seen in younger patients with a history of prior grade II or III gliomas. Inclusion of molecular parameters in treatment algorithms is thought to have a significant impact on prognosis[14]. The prognostic differences between grade II and grade III gliomas have traditionally been considered highly significant[15]. However, recent studies suggests a more similar prognosis in IDH-mutated grade II and grade III gliomas[16]. Furthermore, proposals to treat IDH-wildtype grade II and grade III tumors as GBMs have emerged[14].

Thus, the status of IDH-mutation is significant for prognostics; however, optimal therapeutic strategies to target the mutated subsets of gliomas are currently undecided. In addition to IDH-status, a co-deletion of the short arm of chromosome 1 and long arm of chromosome 19 (1p/19q co-deletion) is a molecular marker for grading of oligodendrocytic gliomas[11]. This marker is strongly suggestive for grade II and III oligodendrogliomas, and is associated with improved survival[17].

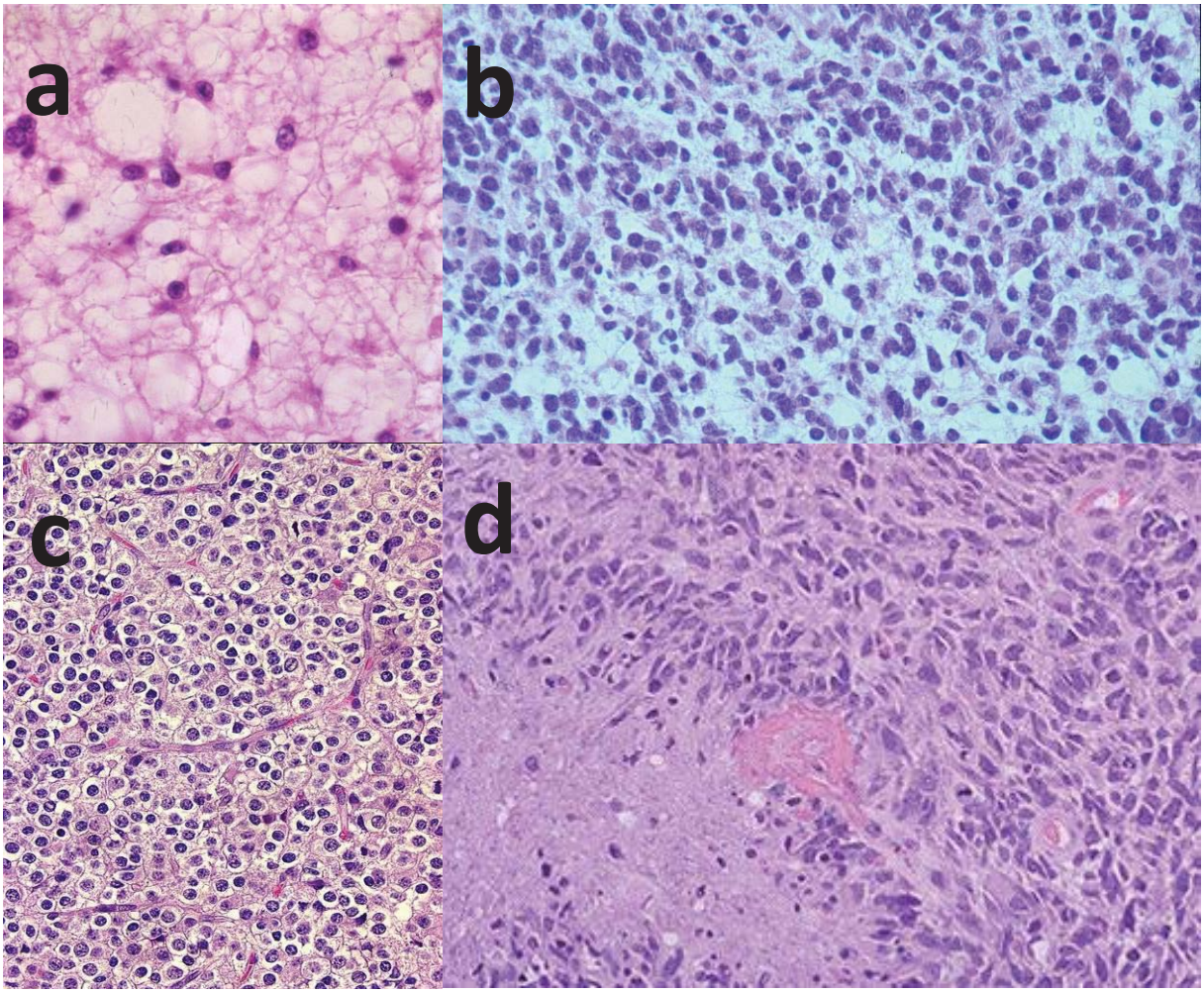

Figure 2: Different glioma types shown with typical histopathological presentation. Grade II diffuse astrocytoma (a); Grade III anaplastic astrocytoma with increased pleomorphism and increased mitosis (b); Grade II oligodendroglioma with typical chicken-wire pattern (c); GBM with increased atypical mitosis (d). Courtesy of Dr. David Scheie, Rikshospitalet, Oslo University Hospital.

1.1.2 Treatment of high-grade gliomas

The standard treatment for HGGs gives a median survival time of 12-15 months for GMBs and 2-5 years for grade III gliomas[2,18]. The standard treatment is multimodal and includes radical surgery, RT and chemotherapy. The prognosis of WHO grade II gliomas is better than HGGs. However, they grow diffusely in the brain and are not considered curable as they progress or become secondary GBMs over time.

Surgery

The diffuse infiltrative nature of gliomas makes removal of the whole tumor impossible. Attempts to remove the entire tumor by hemispherectomy (removal of half the brain) in the 1920s proved pointless as the tumor still recurred on the contralateral side later[19,20]. Surgery is indicated in almost all patients with HGG at some time during the course of the disease. Due to the subacute presentation and, often, continuous neurologic deterioration at diagnosis, early surgery is preferable. Surgery prolongs OS and is needed for histological diagnosis. In addition, symptomatic relief and increased quality of life are known effects of surgery in HGG patients[21]. The extent of surgical resection, with preservation of eloquent neurologic function, is a known prognostic marker for OS. A significant correlation between resection grade and OS has been reported with an OS of 11.0, 9.3 and 2.5 months in complete resection (removal of 100 % of the contrast enhancement (CE) seen on MRI), partial resection (less than 100 % of the CE on MRI) and biopsy respectively[22]. Several studies have found similar results[23–25]. The extent of surgical resection is, however, not clear. The terms “complete resection” and “gross total resection” are used interchangeably in different studies. No visible tumor left at surgery, no CE on the postoperative MRI or resection of more than 90% of the CE on

postoperative MRI have all been used to define gross total resection. An OS benefit has been described at 78% resection of the CE (12.5 months) and OS increased stepwise at 80%, 90% and 100% resections respectively (12.8, 13.8 and 16.0 months)[21]. More radical surgery by removal of the edema surrounding the CE has shown further benefit in survival compared to only removal of the CE (20.7 vs. 15.2 months)[26].

Radiotherapy

The diffuse growth of gliomas leads to microscopic disease in the parenchyma of the brain adjacent to the gross tumor. Ionizing radiation damages the cancer cells leading to cell death directly or by inducing genetic changes[27]. All patients are offered RT and an increased median OS from 4-5 months with surgery alone to 10-12 months was demonstrated by adding postoperatively RT in the 70s[28,29]. These studies used whole-brain radiotherapy due to the knowledge of the infiltrative nature of the disease and the lack of image-based radiation planning technology[28]. 70-90 % of all tumor recurrence happens within a margin of 2-3 cm of the original tumor and localized (stereotactic) radiation was in the 80s and early 90s shown to lead to decreased side effects and equal OS compared to whole brain RT[30]. Standard dosage today is a total of one daily fraction five times weekly for six weeks. Grade III gliomas receive 1.8 Gy each fraction and GBMs receive 2.0 Gy for a cumulative dose of 54 Gy and 60 Gy respectively. This treatment approach is based upon studies of three cohorts from the Brain Tumor Study Group collected between 1966 and 1978[31,32], where an increase in total radiation dose gave an increase in median life span of 28 weeks for 50 Gy, 36 weeks for 55 Gy and 45 weeks for 60 Gy[33]. Increasing the dose beyond 60 Gy has not shown increased survival[34].

Chemotherapy

Chemotherapy in cancer treatment targets the rapid division and fast growth of cancer cells[35]. Traditionally, nitrosoureas (e.g. lomustine) were used as a first line chemotherapy adjuvant to RT in HGGs because of their excellent blood-brain barrier (BBB) penetration properties. Early studies of nitrosoureas showed a small increase in OS[36,37]. In 2005 the alkylating agent temozolomide (TMZ) concomitant and adjuvant to fractioned RT was shown to further increase OS in GBMs[2]. This treatment regime is called the Stupp protocol. Combination treatment of TMZ daily and RT in doses as described above with additional six cycles of adjuvant TMZ increased OS from a median of 12.1 to 14.6 months. The six adjuvant TMZ cycles are currently offered starting four weeks after completing radiochemotherapy. Each cycle consist of TMZ given daily for five days followed by 23 chemotherapy-free days. GBMs with a methylated promoter in the gene for the DNA enzyme O^6-methylguanine-DNA methyltransferase (MGMT) are particularly susceptible to TMZ[3]. No randomized controlled trials have investigated the effect of further TMZ in patients responding to the first six cycles. Some centers practice 12 cycles in patients who otherwise tolerate the therapy and as many as 101 adjuvant cycles have been reported[38].

Treatment of recurrent glioma

Recurrence is inevitable even following radical surgery and radiochemotherapy, due to the invasiveness of HGGs. Repeated surgery in recurrent GBMs lead to increased OS from 8.6 to 18.4 months in a non-randomized, carefully selected sample[39]. Re-irradiation has been used with success in a cohort analysis, with a median survival of 21 months after primary diagnosis of GBM[40]. The effect of concurrent chemotherapy is more

elusive[41]. In MGMT promoter methylation the re-use of TMZ seems advantageous[42]. In the US and many European countries use of the anti-angiogenic monoclonal antibody bevacizumab for recurrent disease has increased in the last years. Despite promising initial results in phase II trials and impressive radiographic response[43,44], no increase in OS from bevacizumab was seen in a meta-analysis of all available trials[45]. Several novel treatment studies of recurring GBM use nitrosoureas in the control arm[46]. In this setting, the nitrosoureas have shown comparable effect to novel agents[46,47], leading to increased use due to its relative lower cost. Thus, nitrosoureas are the most widely accepted chemotherapeutic agents for recurrent GBM[48].

1.2 Magnetic resonance imaging

MRI is the preferred imaging modality in initial diagnostics and follow-up of gliomas. A detailed description of MRI is beyond the scope of this thesis. The topic is described in details in the many textbooks covering the field[49,50].

1.2.1 Basics of magnetic resonance imaging

Magnetic resonance is based on the spin angular momentum (spin) properties of certain atomic nuclei. Nuclei with non-zero spin absorb and re-emit electromagnetic radiation when exposed to a magnetic field [51,52]. This phenomenon, known as nuclear MR (NMR), reflects the fact that the interaction only occurs at a specific frequency which is proportional to the strength of the magnetic field and the magnetic properties of nuclei possessing spin. In MRI, it is often the single proton nuclei of the hydrogen atom (^{1}H) which is utilized, due to the high natural abundance of hydrogen/water in the human body. The proton can assume two distinct energy states when exposed to an external

magnetic field; a low-energy state (parallel to the magnetic field) and a high-energy state (anti-parallel to the magnetic field). In addition to the spin alignment, the spins rotate around their own axis, called precession. In a steady-state condition, there is a slight bias towards more spins on average being aligned with the external magnetic field, resulting in a net magnetic moment from all spins aligned with the applied magnetic field. The effects observed in MRI are readily explained in terms of classical physics since we are observing the bulk effect of a very large number of spins. The collective effect of all nuclear spins can then be described in terms of a single net magnetization (**M**) which tends to be aligned with the static magnetic field ($\mathbf{B_0}$) and precessing around the main field axis with an angular frequency which is proportional to $\mathbf{B_0}$. To observe this net magnetization, the spin system needs to be disturbed from its equilibrium condition by applying a second, much weaker magnetic field ($\mathbf{B_1}$) in a direction perpendicular to the main magnetic field. This second field is applied in the form of radio frequency (RF) pulses where the frequency of the RF pulses matches the precession frequency of proton spins and is referred to as excitation. The disturbed magnetic signal is then detected by conducting coils placed close to the body area of interest. The spin system returns to its steady state energy state in a process called spin relaxation. This can be observed as a gradual decay of the detected signal in the detector coils. Spin relaxation is described by two separate (but not independent) processes referred to as T_1- and T_2-relaxation. T_1-relaxation (also called spin-lattice or longitudinal relaxation) refers to the gradual re-alignment of the net magnetization vector along the axis of the main magnetic field following the application of an RF-pulse excitation whereas T_2-relaxation refers to the gradual signal loss (as measured in the coil) as a result of slight variations in the precession frequency of individual spins due to both interactions at the nuclear level but also due to slight variations in the effective static magnetic field resulting in spatial

differences in the frequency of precession and resultant loss of phase coherence in the measured signal.

To spatially encode the NMR signal, additional position-dependent magnetic fields (field gradients) are introduced so that the precession frequency of the measured magnetization becomes position dependent. By also making the excitation RF-pulses frequency selective, it is possible to selectively only excite spins at a certain spatial position and further to decode the unique position of the NMR signals, by mathematical analysis of the frequency- and phase information in the measured signals. To obtain enough information to spatially encode the measured NMR signals, multiple RF-pulses must be applied under different field gradient conditions, and this combination of multiple RF-pulses under varying gradient conditions is referred to as a 'pulse sequence'. MR sequences can, at a top level, be characterized according to their sensitivity to the two relaxation processes described earlier. Sequences designed for optimal sensitivity to the T_1-relaxation process, T1-weighted (T1w) sequences, are best suited for accurate delineation of anatomical structures whereas T2-weighted (T2w) sequences are generally more sensitive to pathological processes (figure 3). This differentiation is, however, not always clear-cut and a main challenge in MRI is to identify the optimal MR sequence type and parameters for a given diagnostic indication.

MRI is a unique modality in that it combines high spatial resolution with excellent soft tissue contrast in the brain. In addition to high resolution structural imaging, MRI can be made sensitive to a large variety of biophysical properties. In particular, dynamic MRI (rapid sampling of the imaging volume repeatedly) can assess tissue function and hemodynamic properties by means of a large variety of different techniques, either

involving the injection of a contrast agent (CA) or by using endogenous contrast mechanisms. These methods are collectively known as functional MRI methods.

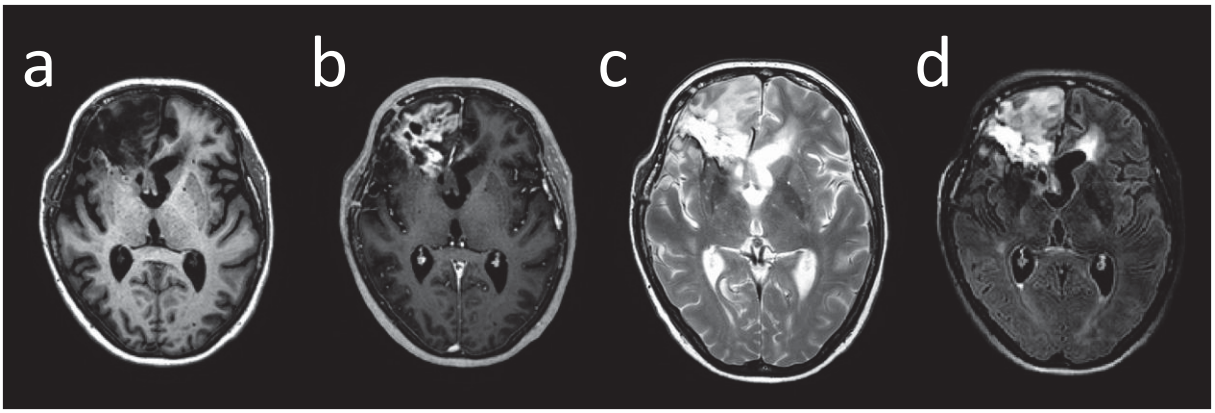

Figure 3: Structural MRI of a GBM in the right frontal lobe. T1w images before (a) and after (b) the administration of a gadolinium based contrast agent (GBCA) are shown on the left side. T2w image (c) and Fluid Attenuated Inversion Recovery (FLAIR) image (d) to the right. Note how the tumor appears dark on the T1w image before contrast (a) and the heterogeneous enhancement pattern after GBCA administration with a mix of enhancing and non-enhancing regions (b). Periventricular high intensity lesions are easier recognized in the FLAIR image compared to T2w image due to suppression of the T2w high intensity cerebrospinal fluid signal.

1.2.2 Contrast agents in magnetic resonance imaging

Originally CAs in MRI were used in conjunction with structural imaging for improved delineation of pathology[53]. Experience from computer tomography (CT) showed that CE helped in differentiation of edema and tumors in both the brain and the rest of the body[54]. In MRI, several paramagnetic ions (manganese (Mn), iron (Fe), chromium (Cr) and gadolinium (Gd)) were investigated, and the first Gd-based CA (GBCA) was approved in 1988 for clinical applications[55]. A paramagnetic ion contains metal ions with unpaired electrons that create a large magnetic moment, as the magnetic moment of an electron is about 700 times larger than that of a proton. Unlike the iodine-based CAs used in CT and X-ray, the CAs used in MRI are not directly visualized in the images, but observed indirectly through their effect on T_1-, or T_2-relaxation times. Most clinically

approved CAs are low molecular weight chelates with Gd used as the paramagnetic ion[56], and all CAs mentioned in this thesis are GBCAs unless specified otherwise.

CAs induce both T_1-, and T_2-shortening in tissue, and the imaging effect of this relaxation enhancement depend strongly on the tissue properties, as well as on the MRI sequence used[57]. A linear relationship between T_1 relaxation rate change and the CA concentration is usually assumed, so that:

$$R_1 = \frac{1}{T_1} = \frac{1}{T_1(0)} + r_1[Gd] \qquad [1]$$

where T_1 is the spin lattice relaxation time (unit s) at a Gd-concentration [Gd] (unit mmol/L = mM) and $T_1(0)$ is the baseline T_1 in tissue. R_1 is the relaxation rate (unit s^{-1}) and r_1 is the in vivo spin lattice relaxivity constant (unit $mM^{-1}\ s^{-1}$) for the specific CA used. The same relationship applies for T_2 relaxation:

$$R_2 = \frac{1}{T_2} = \frac{1}{T_2(0)} + r_2[Gd] \qquad [2]$$

where R_2 is the relaxation rate, r_2 is the in vivo spin-spin relaxivity constant for Gd, [Gd] is the concentration, T_2 is the spin-spin relaxivity time and $T_2(0)$ is the baseline T_2 in tissue.

In addition to the linear increase in R_1 and R_2, transverse relaxation is further enhanced. Susceptibility effects arise from the macroscopic effects of the bulk magnetic moment of the CA, resulting in increased R_2^*. This effect is not dependent upon direct interaction between the protons and the CA. This susceptibility effect is particularly dominant when the CA is confined to a small compartment, giving rise to large magnetic field gradients outside the CA containing compartment[58]. The R_2^* effect can be described similar to Equation 2. It should be noted that, in addition to the linear dependence described

above, non-linear relaxation effects may also contribute to both T_1-, and T_2/T_2*-relaxation, depending on tissue structure, CA concentration and water dynamics.

The use of GBCAs has generally been considered relative safe with reports of adverse allergic reactions at 2.4 % or lower and serious adverse reactions at 0.03 % or lower[55]. In 2006 the administration of GBCAs in patients with severe impaired renal function was linked to the potentially deadly disease nephrogenic systemic fibrosis. This led to restricted use of GBCAs and kidney function measurements before administration. Recently, retention of GBCAs has been observed in the brain after repeated injections leading to a safety announcement from the American and European authorities regarding cautious use of GBCAs. The effect of this retention is, at this point, unclear and no harmful effects are so far documented[59].

1.2.3 Perfusion-weighted magnetic resonance imaging

pMRI is part of the functional MRI domain. These functional methods are used to provide (semi) quantitative assessment of functional and biological processes. In the brain, measures of CBV, CBF and capillary permeability are estimated using pMRI[60–63].

pMRI can be performed both by means of a CA administration or using blood as an endogenous contrast using a technique called arterial spin labeling (ASL). Contrast enhanced pMRI refers to sequences where MRI images are acquired repeatedly before- and following a bolus injection of a CA. The dynamic signal is then measured and modeled voxel-vise according to a pharmacokinetic model. In the brain, the CA distribution using existing GBCAs is usually assumed to be purely intravascular in the absence of pathology compromising the BBB. In the presence of BBB damage the CA leaks into the extracellular, extravascular space (EES). In general contrast enhanced

pMRI methods are divided in two groups dependent upon the principal contrast mechanism; Dynamic contrast-enhanced (DCE)-MRI and dynamic susceptibility contrast (DSC)-MRI.

Dynamic contrast-enhanced magnetic resonance imaging

DCE-MRI uses a T1w sequence and is the preferred method in diseases with BBB disruption. The CA leaks through the damaged capillary bed into the EES until the concentration of CA in the interstitium is equal to that of the plasma. This contrast extravasation is determined by the CBF, the surface area of the damaged vessel and the capillary permeability, the latter two commonly denoted the permeability surface area product (PS). CA extravasation is analyzed using heavily T1w imaging techniques since the T_1-relaxivity of CAs is much higher after extravasation, providing high sensitivity to CA leakage combined with a predictable dose-response. The signal change as a function of time is measured and underlying properties of the tissue such as capillary permeability, blood volume and EES volume are estimated using standardized tracer kinetic models. Concentration time curves from different regions of the brain are shown in figure 4.

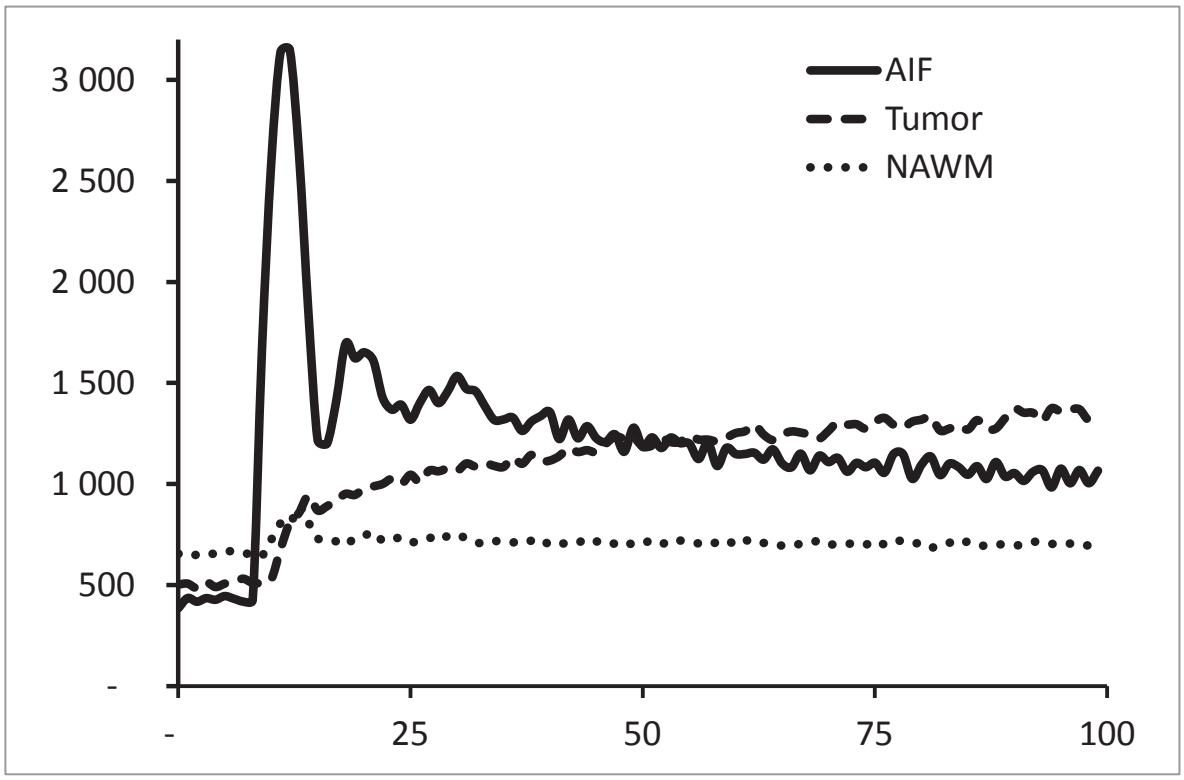

Figure 4: Temporal evolution of the signal intensity after the administration of a GBCA using DCE-MRI. Imaging time-point is shown at the x-axis and signal intensity at the y-axis. The black line is the signal in a large artery. The stapled line is the signal in a brain tumor with damage to the blood-brain barrier. The dotted line is the signal in normal appearing white matter in the contralateral hemisphere of the tumor.

Dynamic susceptibility contrast magnetic resonance imaging

In the brain with intact BBB, T_2*-relaxation dominates due to high degree of compartmentalization of the CA to a small tissue volume (intravascular volume of 2-4% in normal brain)[64]. This results in large local susceptibility differences, and consequent T_2*-relaxation enhancement arising from the enhanced magnetization of the intravascular space due to the presence of Gd. This effect can be captured using DSC-MRI applying echo-planar imaging (EPI) readouts. EPI is a rapid MR acquisition method and commonly used in DSC-MRI due to very high T_2*-sensitivity combined with fast acquisition (high temporal resolution (T_s)), but is susceptible to geometric distortions due to inhomogeneities in the main magnetic field[65].

The T_2*-effect is 'long-range' and does not require direct interaction between the water molecules and the paramagnetic centers. The higher sensitivity of DSC-MRI (steeper dose-response) has therefore made this the method of choice for many perfusion applications in the brain, especially stroke imaging where BBB disruption is not a major issue[66,67]. DSC-MRI is usually analyzed assuming a purely intravascular CA distribution; yielding estimates of CBF, CBV and the ratio of volume to flow reflecting the mean transit time of the tracer through tissue[68,69]. A standardization of CBV and CBF to normal appearing areas in the contra lateral hemisphere is often estimated denoted relative (r)CBV and rCBF[70].

In the presence of BBB disruption, the utility of the DSC-MRI technique is hampered by CA leakage. T_1-relaxivity increases significantly and T_2*-relaxivity generally decreases after CA extravasation due to a larger distribution volume and less CA compartmentalization in the EES; resulting in an unpredictable combination of T_1- and T_2* relaxation effects taking place. The standard kinetic model used to estimate CBF and CBV also becomes invalid in the presence of CA extravasation, yielding erroneous parameter estimations unless corrected for[71]. Different modifications to the standard kinetic modeling have been proposed to correct for the effect of CA leakage in DSC-MRI[71,72]. In spite of the need to correct for CA leakage, DSC-MRI has become an established approach for brain tumor diagnosis. An example of change in signal intensity in different regions in DSC-MRI is shown in figure 5.

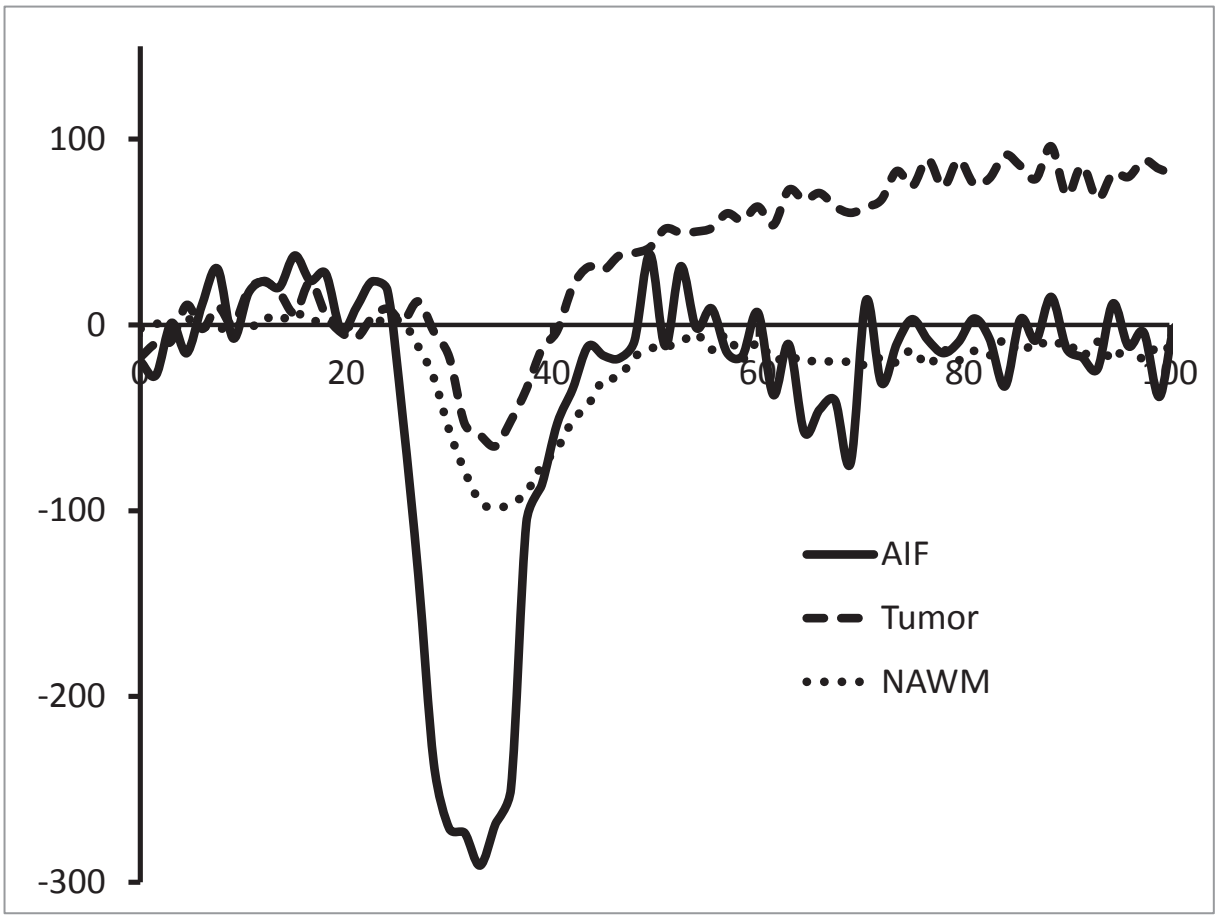

Figure 5: Temporal evolution of the signal intensity after the administration of a GBCA using DSC-MRI. Time points shown on the x-axis and change in r_2* shown on the y-axis. The black line is the signal from a large artery. The stapled line is the signal from a tumor with damage to the blood-brain barrier. The dotted line is from normal appearing white matter in the contralateral hemisphere of the tumor. The signal is taken from the same regions as figure 4.

Tracer kinetic modeling from DCE-MRI

The present work focused on DCE-MRI and the kinetic models used to analyze such data in brain tumors will therefore be discussed in more details below. Many different kinetic models have been proposed, ranging from very simple (few model parameters) to very complex multi-compartment models[73]. A standardization effort, based on three kinetic models introduced almost simultaneously in the early 90s[60,74,75], was made in the late 1990's, resulting in a consensus paper on model selection and parameter notations[76].

The model most frequently used is the extended Tofts model based upon a generalized kinetic model proposed by Kety in 1951[77].

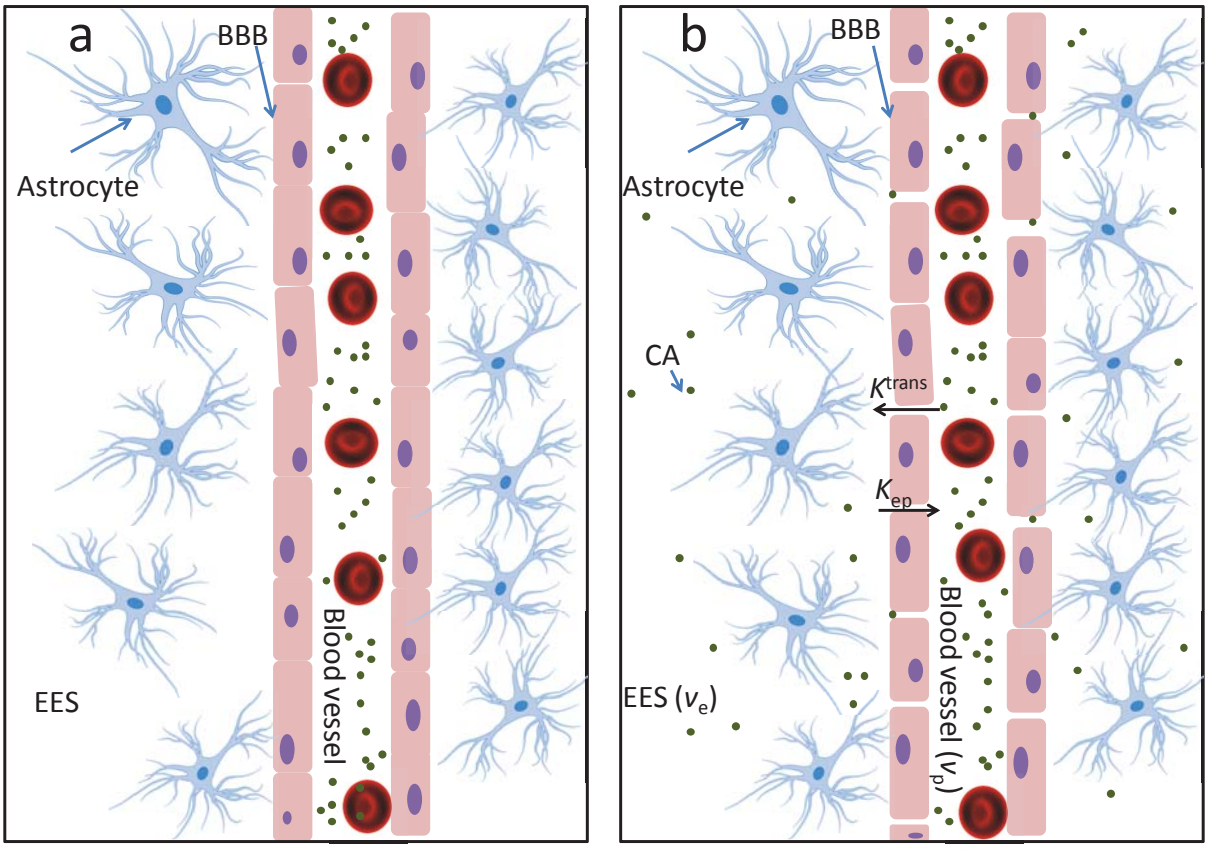

Figure 6: (a) Distribution of GBCA molecules (green dots) in an intact BBB. The distribution volume is in the vessel alone. The right panel (b) shows distribution volume of GBCA molecules in a vessel with pathologic BBB. The GBCA molecules extravasates through the endothelium and into the EES at a rate of K^{trans}. When the molecules enter the EES, they start to leak back to the plasma at a rate of k_{ep}. The fraction of EES in a given area (most commonly voxel) is denoted v_e, v_p is the fraction of plasma.

To describe the kinetics of the tracer in tissue or tumor we define the different tissue compartments constituting the total tissue volume as well as the flux and reflux of the CA between these compartments. Commonly the tissue is divided in three compartments; the blood volume, the intracellular space and the EES as seen in figure 6. The CA is confined to the blood volume or the ESS. All other tissue compartments are considered inaccessible to the CA including the erythrocytes, intercellular space and other none diffusible tissue such as fibrous tissue and membranes. The different

compartments are defined as fractions of total tissue volume in a given MR image voxel. The total tissue volume per voxel is then given by:

$$v_p + v_e + v_i = 1 \qquad [3]$$

$$v_p = (1\text{-hct})v_b \qquad [4]$$

where v_p is the fraction of plasma volume, v_e is the fractional EES, and v_i is the fraction of tissue inaccessible to the CA as described above. v_b is the fraction of whole blood and hct is the hematocrit.

The kinetic parameters K^{trans} and k_{ep} are the CA transfer constant and the rate constant, respectively where $k_{ep} = K^{trans} / v_e$.

The rate equation for the extended Tofts model is given by[77]:

$$\frac{d[C_t(t) - v_p C_p(t)]}{dt} = K^{trans} C_p(t) - \frac{K^{trans}}{v_e}[C_t(t) - v_p C_p(t)] \qquad [5]$$

The solution for $C_t(t)$ is then given by:

$$C_t(t) = K^{trans} \int_0^t C_p(\tau)\, exp\left(-\frac{K^{trans}(t-\tau)}{v_e}\right) d\tau + v_p C_p(t) \qquad [6]$$

where $C_t(t)$ is the total CA concentration in tissue, $C_p(t)$ is the plasma concentration in a feeding artery commonly known as the arterial input function (AIF), v_p is fractional tissue plasma volume, K^{trans} is the CA transfer constant and v_e is the CA distribution volume fraction in the EES. Estimated parameter maps from DCE-MRI and DSC-MRI are shown in figure 7.

Given that $C_t(t)$ and $C_p(t)$ can be measured, equation [6] can be solved for K^{trans}, v_e and v_p using deconvolution or non-linear least squares curve fitting techniques. In our analysis,

we used the method first proposed by Murase whereby equation [5] is linearized by transformation to a matrix expression which can be solved by singular value decomposition to yield estimates of the three kinetic model parameters[78].

K^{trans} is dependent on CBF and PS. In tissues where perfusion is low and permeability is high K^{trans} will be limited by available perfusion. This is referred to as flow-limited condition. In this situation K^{trans} mainly reflects perfusion and not PS product. In the other extreme, PS^s << CBF and K^{trans} then directly reflects the PS product[79]. The extended Tofts model, used in the current work, explicitly assumes permeability limited conditions.

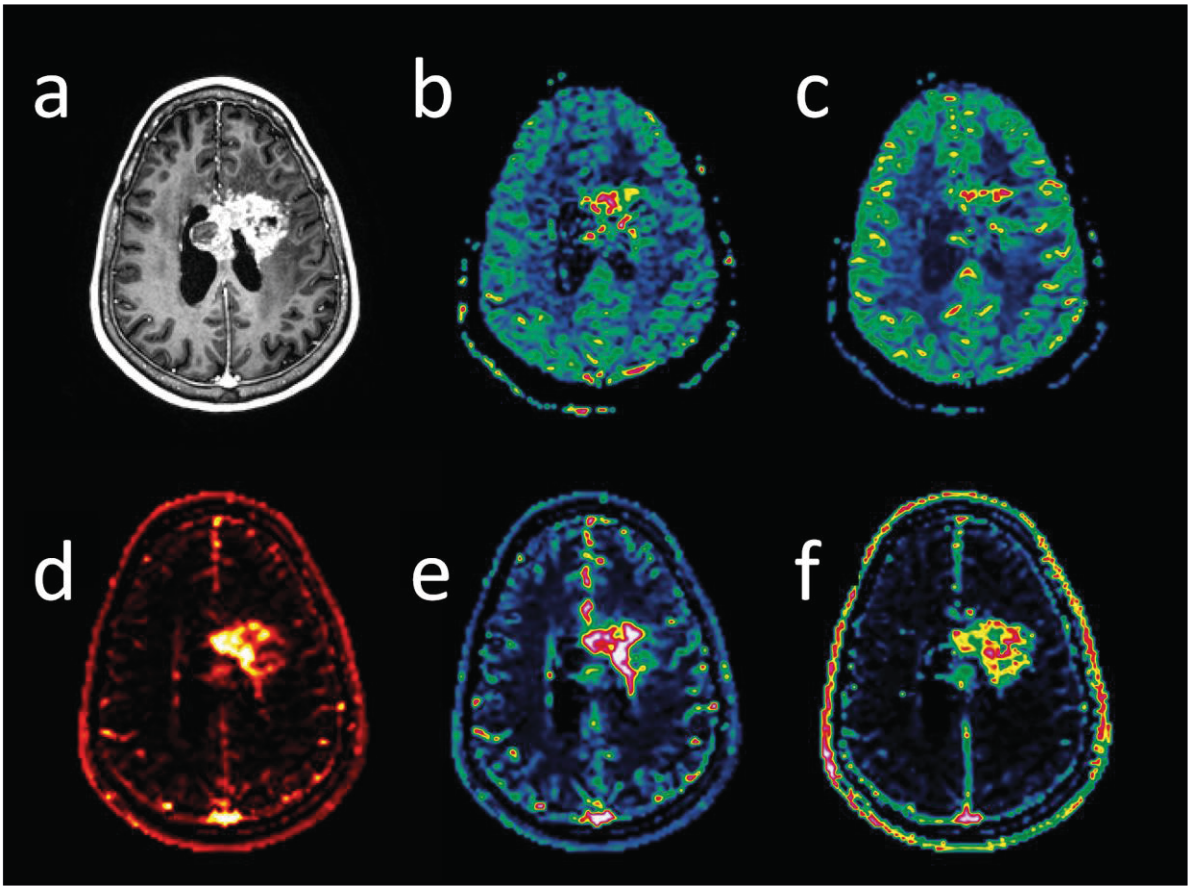

Figure 7: Structural image (a) and estimated parameter maps (b-f) of a patient from the thesis. Structural CE T1w image of the tumor is shown in a. Estimated parameter maps of rCBF and rCBV from DSC-MRI are shown in b and c respectively. From DCE-MRI estimated parameter maps of K^{trans}, CBF and v_e are shown in d, e and f respectively.

Parameter requirements in DCE-MRI

Different methods for measuring the AIF, specific scan parameters and acquisition type all affects the MR signal and derived parameters. In DSC-MRI this has led to the use of normalized parameters yielding perfusion metrics that are more readily compared between subjects and institutions[70]. Such normalization is not generally possible for DCE-MRI in the brain due to zero parameter values in healthy brain. Numerous studies address factors affecting the accuracy and reproducibility of metrics derived from DCE-MRI, including effect of acquisition parameters, applied kinetic model, and analysis approach[70,76,77]. In DCE-MRI, the Quantitative Imaging Biomarker Alliance (QIBA) created a white paper in 2012 outlining the use and quantification in clinical trials[82]. This is an effort to standardize the measurement and estimation of K^{trans} at 1.5 Tesla with a 20 % within-subject coefficient-of-variation. QIBA recommends $T_1(0)$ measurements using 2-7 degree variable flip angles, T_s less than 10 s, ideal slice thickness less than 5 mm and 1-2 mm in-plane resolution and a total measurement time (T_{acq}) of more than 5 min after CA injection for the DCE-MRI sequence (summarized in table 3). There are, however, discrepancies in the published sequences regarding these recommendations (table 3).

The T_s in DCE-MRI is in most studies as short as possible to accurately sample the AIF. This compromises spatial resolution and signal-to-noise ratio (SNR). It was predicted that a T_s in the order of one second is required for accurate AIF determination in DCE-MRI of the breast[83]. Most studies in the brain use a T_s in the 3-10 s range (table 3). Simulations exploring the effect of low T_s and inaccurate AIF sampling have shown larger errors in K^{trans} estimates from incorrect AIF measurement than slow sampling. A recent simulation study showed that K^{trans} was only to a small degree (less than 20 %)

underestimated at T_s rates up to 20s[84]. The same study showed that accurate and reproducible AIF determination is critical for quantitative assessment of kinetic parameters and also for tracing changes over time[84]. The AIF varies due to variations in cardiac output, vessel size of feeding arteries (partial volume effects) and high peak concentrations with rapid changes in CA concentration. Due to the difficulty and lack of consensus in obtaining an AIF, several strategies have been employed. Parker et al. made an experimentally derived population-averaged AIF using the large arteries in the abdomen of 23 cancer patients from a total of 67 visits[85]. This AIF has been used in several studies where an individual AIF was not obtainable[86,87]. However, there is an expectancy that the exact shape of the AIF is dependent on the feeding arteries from which it is derived[85]. The ability to measure the AIF directly from cerebral arteries requires good arterial signal in the DCE-images and a T_s that accurately samples the peak of the AIF. If a low sampling volume or few slices are acquired, large arteries may not be part of the imaging volume. AIFs from small arteries might lead to partial volume effects and severe underestimation of the peak AIF height. Vascular input functions (from large veins), including the superior sagittal sinus have been used, due to the lack of supplying arteries of sufficient size in the acquired sampled volume[88]. The venous signal has a later onset time and an increased dispersion compared to an AIF, with larger signal amplitude due to less partial volume effects. A comparison of different AIF methods in both DCE-MRI and DSC-MRI suggests the use of a carry on AIF. Using double baseline data (two MRI sessions few days apart); i) population AIF, ii) individual AIF and iii) patient specific AIF based on the AIF from the first scan, the studies concluded that the use of a patient specific AIF gave the highest reproducibility of estimated parameters in both DCE-MRI and DSC-MRI[89,90].

In T1w imaging, conversion from change in signal intensity to change in $1/T_1$ requires knowledge of $T_1(0)$ in tissue and further an assumption about negligible transverse (T_2 and T_2*) relaxation effects during the CA bolus[91]. The need for accurate high resolution mapping of a wide range of $T_1(0)$-values and accurate co-registration to DCE-MRI data can be challenging[83]. In clinical routine with the limited time reasonably available, T_1 mapping in DCE-MRI analysis is therefore achieved by rapid imaging methods using one of two established methods; the first method applies an inversion (180 degree) pulse followed by a train of small flip-angle readout pulses to monitor the magnetization recovery to steady state. This method is termed rapid inversion recovery or 'Look-Locker' (named after the two researchers who first described this sequence for T_1-measurements in the 1970's)[92]. In the second method, two or more rapid gradient-echo images with different flip-angles are acquired, enabling estimation of T_1 from the known dependence of MR signal intensity on T_1 as function of flip-angle[93]. The need for $T_1(0)$ data increases total scan time, and brings about the need for image co-registration and additional image processing steps. The added value of using $T_1(0)$ maps in DCE-MRI analysis has thus been questioned[94]. The use of a separately acquired $T_1(0)$ map may potentially also be prone to additional sources of error, such as RF-pulse imperfection leading to spatial bias in the estimated T_1-values, co-registration errors and additional noise from the T_1 measurement itself[95]. If an accurate $T_1(0)$ is not obtainable, a constant $T_1(0)$ value must be assumed for all tissues. This is shown be more stable than calculations of $T_1(0)$[94]. In longitudinal studies, relative change in the estimated parametric values is more robust than individual $T_1(0)$ measurements given stable $T_1(0)$ values. The absolute values are heavily dependent on $T_1(0)$[86].

1.3 Magnetic resonance imaging of gliomas

Clinical imaging of HGG patients before, right after surgery and every third month after end of radiochemotherapy is the standard imaging routine in Norway. This is in line with international recommendations of imaging every 2-4 months after initial radiochemotherapy[96]. A standard protocol includes Fluid-Attenuated Inversion Recovery (FLAIR) imaging, T1w imaging before and after injection of a GBCA, T2w imaging and diffusion weighted imaging (DWI)[97,98]. Conventional MRI provides qualitative data and gives insight in the morphology and progression of the disease.

1.3.1 Structural magnetic resonance imaging in gliomas

In general gliomas are hyperintense on T2w imaging and hypointense in T1w imaging. In WHO grade II tumors these findings are typically homogenous with small mass effect due to slow growth. CE is rarely seen after injection of a CA[99]. In WHO grade III and IV gliomas the MRI findings often reflect the increased malignancy of the tumors. BBB disruption is usually present with CE and a more heterogeneous appearance. In grade III gliomas a patchy CE can be seen while GBMs characteristically have an irregular enhancement with central non-enhancing areas mirroring the large extent of neovascularization around necrotic regions[97]. This highly heterogeneous appearance is the reason for the former name glioblastoma multiforme. The CE is surrounded by vasogenic edema from the breakdown of the BBB and the degree of CE and volume of surrounding edema are closely correlated[100]. To some extent, these MRI findings resemble the features found on the histopathology[97]. Typical findings on structural MRI in gliomas are seen in figure 8. Degree and heterogeneity of CE, necrosis/cyst formation and mass effect are all significantly related to tumor grade[101]. Unfortunately, there are

several exceptions to these general rules and the use of structural MRI for grading is thus limited[99].

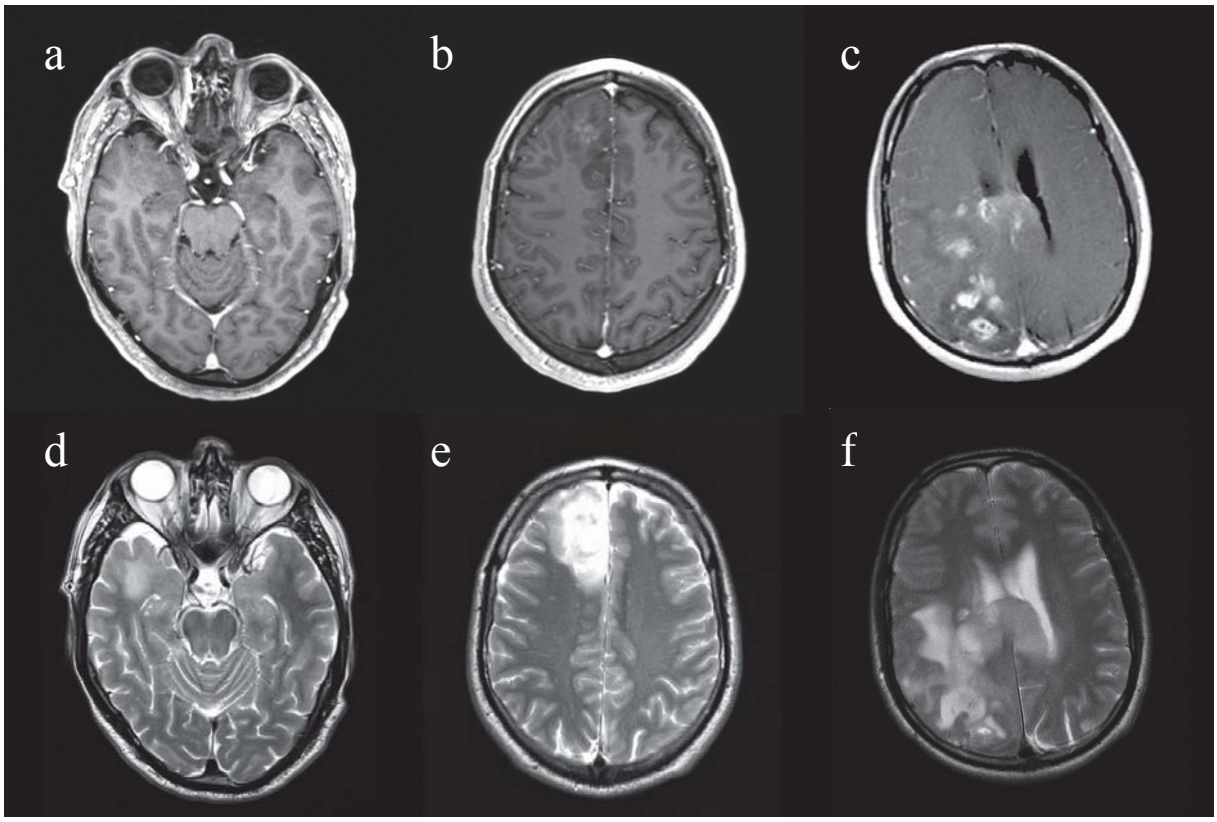

Figure 8: Comparison of imaging findings in a grade II glioma (a and d), a grade III glioma (b and e) and a GBM (c and f). Contrast-enhanced T1w MRI (a-c) and T2w MRI (d-f). No CE is seen in the grade II glioma (a), but some edema in the right temporal lobe is seen in the T2w images (b). In the WHO grade III glioma a patchy CE is seen in the right frontal lobe with surrounding edema (b). Large CE is seen in the T1w images of the GBM (c). The CE is highly heterogeneous with some lesions showing signs of cystic formation and necrosis. Images courtesy of Kyrre Emblem PhD, Department of Diagnostic Physics, Oslo University Hospital.

1.3.2 Response criteria in high-grade gliomas

Treatment assessment of gliomas is typically done by radiologic estimations of growth. Studies have shown that glioma grade and survival is poorly correlated to MRI findings based on conventional images; e.g. size of CE and hyperintensities on FLAIR and T2w images[102,103]. For many years, the gold standard for assessing treatment response was the Macdonald Criteria from 1990[104]. The original Macdonald Criteria were based upon contrast enhanced CT, and tumor size was defined as the product of the maximal cross-

sectional diameter and the largest diameter perpendicular to the enhancing area[104]. Four clusters of disease stages were included; complete response, partial response, stable disease and progressive disease. Use of corticosteroids and change in neurological status were also part of the assessment. Since then, the criteria have been used as a response measurement in glioma studies using the CE on T1w images. In 2000 the Response Evaluation Criteria in Solid Tumors (RECIST) guidelines were introduced to standardize the definition of tumor progression in cancer in general, and to include 3D measurements possible due to advances in CT and MR imaging[105]. These criteria are non-specific for all solid tumors and include specific guidelines for measurement of multifocal tumors, a rarity in gliomas. In gliomas, continued use of the Macdonald Criteria enabled comparison with historical data and thus remained the most widely used method for assessment of treatment response. Recently, the limitations of the McDonald Criteria were reviewed and potential sources of error, such as difficulties in measuring multifocal tumors (although a rarity), inter-observer variability and definition of tumors with large cystic or surgical cavities were pointed out[106,107]. Moreover, better MRI scanners and more advanced imaging methods such as FLAIR and dynamic imaging open up the opportunity for more advanced assessment. The Response Assessment in Neuro-Oncology Working Group (RANO) initiative proposed updated assessment criteria in 2010 and have been the gold standard for the last years[106]. Similar to the McDonald Criteria they use four clusters of disease stages (summarized in table 1). The inclusion of T2w/FLAIR assessment and clearer definitions of MRI measurements are the main differences from the McDonald Criteria. Volumetric assessment is not yet recommended due to lack of standardization and availability[106].

Table 1: Summary of the RANO Criteria.

Criterion	**CR**	**PR**	**SD**	**PD**
T1w CE	None	≥ 50 % ↓	<50%↓ but <25 %↑	≥25% ↑*
T2w/FLAIR	Stable or ↓	Stable or ↓	Stable or ↓	↑
New lesions	None	None	None	Present *
Corticosteroids	None	Stable or ↓	Stable or ↓	NA†
Clinical status	Stable or ↑	Stable or ↑	Stable or ↑	↓*
Response requirement	All	All	All	Any *

The arrows indicate the direction of measured change from last exam. Abbreviations: RANO: Response Assessment in Neuro-Oncology, CR: complete response, PR: partial response, SD: stable disease, PD: progressive disease, T1w: T1 weighted. T2w: T2 weighted, CE: contrast enhancement, FLAIR: fluid-attenuated inversion recovery, NA: not applicable. * Progression occurs when this criterion is present.

The RANO Criteria point out that advance techniques such as DSC,- DCE,- and DWI-MRI may prove to be valid contributions to treatment response evaluation or differentiation of non-enhancing tumor from other sources of increased signal on FLAIR images in the future[106]. However, validation through multiple trials is required before these techniques are incorporated in conventional clinical assessment of gliomas.

1.3.3 Imaging of radiation-induced injury and pseudoprogression

Radiation-induced injury to the brain is traditionally divided in three types; acute (during RT), subacute (up to 12 weeks after RT) and late (3-12 months after RT). MRI is usually normal in acute radiation-induced injury making this a clinical diagnosis. Imaging findings in subacute radiation injury are caused by vasodilatation and edema from BBB damage and are usually transient. Late radiation injuries are often irreversible and progressive and include radionecrosis, leucoencepalopathy and other vascular lesions[4]. Radiation induced necrosis is rarely seen today due to utilization of fractionated RT and smaller fractions during a longer treatment period. However, it may

still occur in hyper-fractionated RT regimes, in patients with large fraction areas or in re-irradiation[108]. Pseudoprogression is a transient treatment related increase in CE and/or edema on MRI without tumor activity[109]. It occurs with or without signs of necrosis in biopsies of the lesion[110]. Image findings in pseudoprogression mimics finding in subacute/late radiation-induced injury and disease progression making the distinction between the three entities difficult[111]. It is typically seen on MRI days to six months after radiochemotherapy which is similar to the occurrence of subacute and late radiation necrosis[108,112]. Pseudoprogression was first described in phase III trials of TMZ where a subgroup of patients showed progression on the first MRI after RT and later spontaneously stabilized or got better for at least six months[113]. This led to the conclusion that progressive disease at MRI three months after RT end should not be interpreted as recurrence. Pseudoprogression is a radiological entity and has been reported in patients receiving RT, radiochemotherapy and immunotherapy in metastatic brain cancer. Thus, transient radiation-induced injury can only explain some of the cases of pseudoprogression. Pseudoprogression is reported in 20-30% of patients treated with the Stupp regime[114], and is found more frequently in patients with MGMT promotor methylation[115]. As mentioned in Section 1.1.2. MGMT is a known factor for better effect of TMZ, with an average increase in OS and time to progression. Thus, the distinction between progressive disease and pseudoprogression is important for the prognosis, unfortunately, this is not readily possible by conventional MRI[4,109].

1.3.4 Perfusion magnetic resonance imaging in gliomas

The utility of pMRI for detection, grading and prognostication of gliomas is proven in multiple studies. Perfusion imaging with DSC-MRI is helpful in preoperative glioma grading[116]. LGGs typically have normal values of CBV compared to normal-appearing

brain tissue (rCBV=1). Conversely, regions of increased rCBV are found in HGGs. Regions of high rCBV have been proposed to use as biopsy targets for more accurate diagnostics if a complete resection of the tumor is not possible. Moreover, elevated rCBV values, as a sign of transformation from LGG to HGG, have been found up to one year earlier than the appearance of CE in T1w images[117]. Similar to in DSC-MRI, higher tumor grade is associated with elevated estimated parameters from DCE-MRI[118]. As discussed in Section 1.2.3., DCE-MRI is advantageous in gliomas with CE on T1w MRI and assessment of the transfer constant K^{trans} is of particular interest in HGGs. In a study trying to differentiate between recurrence and pseudoprogression in GBMs, both mean and 90 percentile histogram values of K^{trans} and v_p were higher in the recurrence group[119]. Similar results were seen in a prospective study, where high K^{trans} and v_e were found in GBM patients with progressive disease compared to pseudoprogression[120]. The prognostic value of DSC-MRI and DCE-MRI is discussed later in Section 1.4.

There are some limitations to pMRI for clinical use. First, most research in pMRI is from single center studies. Moreover, standardizing cutoffs/recommendations of the estimated parametric values is challenging. In DSC-MRI normalization to normal-appearing brain in the contralateral hemisphere has been used in an effort of standardization, showing reported values in the literature that are similar[121]. Due to the intrinsic need for BBB leakage to measure meaningful K^{trans} –values, normalization is not done routinely in DCE-MRI where K^{trans} should be close to zero in normal brain tissue. This leads to discrepancies between reported DCE-MRI parameters in the litterature[121]. In addition, choice of statistical method varies extensively between studies. Some studies use the CE as a Region-of-Interest (ROI) and analyze distributions of histograms within this ROI. Another approach visually inspects the parametric maps and places

small ROIs in areas with the highest parameter values, commonly referred to as the hot-spot method. The latter method suffers from inherent user dependence and the first method poses challenges in defining the tumor and is inherently time consuming. A selection of DCE-MRI studies is shown in table 3 with examples of estimated parameter values, T_s, T_{acq} and post-processing procedures. Differences in the estimated parameter values are apparent despite similar T_s and T_{acq}. Moreover, AIF estimation approach, choice of ROI statistics and variable parameter reporting make comparisons challenging. Although DCE-MRI is proven to be a useful tool to characterize endothelial permeability and related kinetic properties, there are several challenges obstructing widespread clinical use of the method.

1.4 Prognostics in gliomas

The prognosis for HGG is dire despite a multimodal treatment approach, and less than 50% of patients live a year after the time of diagnosis of GBM[122]. LGGs have a better prognosis with a median survival of eight to nine years[123]; however, transformation to secondary GBM is seen in a significant part of LGGs (see Section 1.1.1). While IDH-mutated GBMs have a better median OS than IDH-wildtype (27.4 vs. 14.0 months, respectively), prognosis is still dismal compared to other cancer type[124].

Several factors influence the predicted OS (table 2). An observational study looking at different prognostic factors in 660 GBM patients found that young age (significant for cohorts younger than 40 and 60), Karnofsky Performance Score (KPS)>70, adjuvant chemotherapy and high resection grade predicted improved survival[125]. A study investigating outcome in 565 HGG patients found similar results[126]. As mentioned in Section 1.1.2, surgery, RT and chemotherapy all increases OS individually. Recently, in

accordance with the new WHO grading of gliomas, various molecular markers have been recognized that have prognostic properties. In addition to IDH mutation, patients with methylated MGMT have shown increased effect of radiochemotherapy and higher OS compared to RT alone in GBMs (21.7 vs. 14.0 months)[3,127,128].

Table 2: Key prognostic factors in high-grade glioma

	Positive	Negative	OS (months)
Clinical factors			
Age	<40	>60	17.7-9.0[126]
KPS	>70	<70	
Resection grade	GTR	STR/biopsy	11.0-9.3/2.5[22]
Radiation therapy	RT	No RT	11 – 4.5[28]
Chemotherapy	TMZ	No TMZ	14.6-12.1[2]
Molecular factors			
MGMT status	Methylated	Un-methylated	21.7-12.7[3]
IDH-status	Mutated	Wildtype	27.4-14.0
Imaging factors			
Postop CE	Thin linear	Thick linear/nodular	20.3-14.4/10.6[129]
rCBV	Low	High	
K^{trans}	Low	High	
ADC	High	Low	

Abbreviations: OS: Overall survival, KPS: Karnofsky performance score, GTR: gross total resection, STR: subtotal resection, RT: radiation therapy, TMZ: temozolomide, IDH: isocitrate dehydrogenase, MGMT: O^6-methylguanine-DNA-methyltransferase, postop CE: postoperative contrast enhancement, rCBV: relative cerebral blood volume, K^{trans}: transfer constant, ADC: apparent diffusion coefficient.

As discussed in chapter 1.4, MRI is the modality of choice in gliomas and prognostic markers for survival are highly researched. Most studies are published on HGGs/GBMs. The prognostic value of MRI before treatment is uncertain. In a study of treatment-naïve GBMs, clinical parameters (age, sex, KPS and resection grade) outperformed estimated parameters from MRI[130]. Shorter OS has been associated with higher values of K^{trans} and v_p independent of glioma grade in preoperative DCE-MRI[131]. Thick linear enhancement (a several voxels thick line of CE in the rim of the surgical cavity) on post-operative MRI

within 48 hours after surgery predicted the same prognosis as nodular enhancement (i.e. sub-total resection)[129], emphasizing the importance of a complete surgical resection.

The prognostic value of structural MRI and the RANO Criteria during and after radiochemotherapy is undecided. A recent study found better OS in patients with complete response according to the RANO Criteria compared to the other response groups combined[132]. However, when the complete responders were compared to patients with stable or partial response, no difference was found (i.e. not progressive disease). Similarly, a study including whole tumor volumetry found worse prognosis in tumors with more than 5% volume increase at 3 and 5 months after radiochemotherapy[133]. Structural and functional MRI metrics longitudinally analyzed predicted OS and progression-free survival (PFS) before and after RT[134]. In this study tumor volume from T2w imaging was significant both before and after RT for OS and rCBV and CBF was significant for PFS after RT end. This suggests that different parameters are sensitive at different time-points during treatment and disease progression.

Prospective markers in gliomas have mostly revolved around pseudo-biological markers from functional MRI. Biomarkers are defined by the National Institutes of Health Biomarkers Definitions Working Group as a "characteristic that is objectively measured and evaluated as an indicator of normal biological processes, pathogenic processes, or pharmacological responses to therapeutic intervention"[135]. An example is functional diffusion maps using DWI, where increase in apparent diffusion coefficient (ADC) during treatment is associated with treatment response[136]. The functional diffusion maps have equal predictive value as radiographic response using the MacDonald Criteria and is validated as a biomarker for cellularity[137,138]. However, the method has been criticized

because of the voxel-by-voxel analysis which demands rigorous co-registrations of images. Furthermore, pMRI shows prognostic potential in several studies. In DSC-MRI, rCBV is the most promising metric[139]. A cutoff of rCBV higher than 1.75 strongly predicted shorter PFS in DSC-MRI in a large study of gliomas of all grades[140]. The cutoff was not significant for OS. Cutoffs of rCBV 2.00-5.79 have been reported in the literature for significant OS prediction[141–143]. While elevated rCBV is a known negative prognostic marker in gliomas, the clinical utility of rCBV measurements is challenged by overlapping cutoff values presented in the literature and across grades[72]. Of the prognostic marker from DCE-MRI, K^{trans} is the parameter most often reported in the literature. As mentioned above, preoperative K^{trans} and v_p were higher in patient with lower OS[131]. Likewise, increased maximum K^{trans} values in patients are associated with worse prognosis[144]. Several histogram percentiles were significant for shorter OS in patients with high K^{trans} and v_e in a study investigating a multitude of histogram metrics[145]. However, direct comparison of parametric values in DCE-MRI is more difficult than in DSC-MRI due to the lack of relative values and larger variations in reported metrics.

Studies combining clinical and/or imaging biomarkers are emerging. Combining K^{trans} and CBV from DCE-MRI and DSC-MRI respectively have shown increased prognostic value compared to either parameter alone[144]. Similarly, patterns of combined ADC and CBV in tumors have predicted OS[146]. Moreover, imaging can be used to stratify prognosis; a recent study found that patients from a subgroup with MGMT methylation with high CBF measured by ASL had statistically longer PFS[147]. An index of K^{trans}, rCBV and measurements of circulating collagen IV, created in an effort to measure the

normalization of vasculature, correlated with OS and PFS in recurrent GBMs treated with an angiogenesis inhibitor[148].

Unfortunately, some challenges for widespread use of MRI in prognostics restrict the use in clinical practice as mentioned in Section 1.4.. First, the timing of imaging is different between studies. Imaging is performed at time of diagnosis, after surgery, after radiochemotherapy and during follow-up. The timing of this imaging is not clear, and the optimal time for imaging might vary between the different imaging markers. Second, some studies look at image findings at one time point while others look at serial change in metrics within patients. This makes comparisons of studies more difficult. Third, there is a lack of standardization of MRI sequences. It has been argued that to obtain maximum accuracy from a dichotomized biomarker, the optimal cutoff value should be based on data generated at a given site[149]. All of these issues make comparisons between centers and publications difficult and further efforts in standardization of both MRI sequences and analysis methods are clearly warranted.

1.5 Summary of introduction

HGG remains the deadliest form of primary brain cancer, in spite of intense efforts in developing therapies. Despite aggressive treatment protocols, the prognosis is generally poor. Structural MRI using the RANO Criteria is the current gold standard for treatment assessment, but difficulties in differentiating recurrence from treatment related necrosis is a major problem. pMRI shows promise as a supplement to structural imaging for improved prognostics and in distinguishing pseudoprogression from recurrence. However, widespread use of pMRI is hindered by a lack of standardization and challenges in longitudinal and cross-sectional reproducibility. Hence, this thesis focuses

on methodological considerations in the analysis of DCE-MRI in HGGs and the evolution and prognostic value of derived metrics from DSC-MRI-, and DCE-MRI in early OS assessment.

Table 3: Overview of reported values of estimated kinetic parameters, sequence parameter and analysis methods from DCE-MRI in the literature.

Study	Patients/ Scans	Glioma grade	K^{trans}	k_{ep}	v_e	v_p	T_s (sec)	T_{acq} (min)	Resolution (mm)	KM	Tesla	T_1 mapping	AIF	ROI
QIBA[82]							<10	>5	<2x2x5	STM	1.5	MFA	Individual	Median
Larsson[150]	15/101	3/ 4	0.040	0.3	15.9	1.1	2.1/3.4	5:40	2x2x4	ETM	3	Set	Individual	Median
Zhang[151]	8/8	4	0.214	0.07	72.2	3.4	4	6	0.8x1.25x5	ETM	1.5	MFA	Individual	Mean
Harrer[152]	18/18	3/4	0.028-0.142				6	6	2x2x6	ETM	1.5	MFA	Generated	Median
Bisdas[153]	22/22	4	0.09		24		7	5	1.7x1.7x4	ETM	3	MFA	Generated	Mean
Ulyte[154]	49/49	4	0.13	0.46	0.42	13	6	5	1.7x1.7x4	ETM	1.5	MFA	Individual	90 percentile
Bonekamp[144]	37/37	4	0.32	1.93	37		17/12	5:06/4:24	0.9x0.9x3/5	ETM	3	Set	Generated	Maximum value

Abbreviations: DCE-MRI: dynamic contrast-enhanced magnetic resonance imaging,, T_s: temporal resolution, T_{acq}: total acquisition time, KM: kinetic model, AIF: arterial input function, ROI: region-of-interest, QIBA: Quantitative Imaging Biomarkers Alliance. STM: standard Tofts model, MFA: multiple flip angle, ETM: extended Tofts model.

2 *Aim of this thesis*

The aim of this thesis was to investigate key parameters in acquisition and analysis of DCE-MRI in HGGs and compare the prognostic value of DCE-MRI to that of structural imaging and DSC-MRI in early OS prediction.

Specific aims:

Paper I: To systematically investigate, both through simulations and in clinical data, the effect of varying temporal resolution and total sampling duration on the ability to estimate standard kinetic parameters in DCE-MRI.

Paper II: To measure the temporal evolution of $T_1(0)$ in HGGs and assess the necessity of baseline T_1 measurements in longitudinal analysis of DCE-MRI in HGGs for accurate parameter estimation.

Paper III: Investigate if functional pMRI-derived metrics can aid in improving the prediction of OS in GBM patients compared to conventional volumetric or radiologic assessment by the RANO Criteria alone. Furthermore, to assess the temporal trends of estimated parameters derived from pMRI by both DCE-MRI and DSC-MRI, and investigate differences in their predictive value.

3 Material and methods

3.1 Overall design

The papers included in this thesis are part of a prospective HGG treatment monitoring study conducted at The Intervention Centre, at Oslo University Hospital Rikshospitalet. 27 patients with histologically confirmed HGG were recruited at the Norwegian Radium Hospital before the start of radiochemotherapy. Of the 27 patients, 23 had GBM. The patients with WHO grade III tumors were excluded from the last paper due to the small subject number. All patients underwent MRI prior to (baseline scan), every second week during and two weeks after completion of radiochemotherapy. Three-monthly scans were performed upon completion of radiochemotherapy until expiration or disease progression leading to drop-out of the follow up. All patients were clinically assessed by a Karnofsky Performance Score (KPS) at each imaging time-point[155].

3.2 Ethical statement:

The study was conducted according to the Declaration of Helsinki[156]. The Regional Ethical Committee approved of the study (reference number 2009/1867b) and informed consent was signed before inclusion.

3.3 Imaging protocol

The MRI system used was a Philips Achieva 3 T (Best, the Netherlands) using an eight-channel head coil (InVivo, Gainsville, Fl, US). The same MRI protocol was used throughout the study and included structural and dynamic imaging, including: 3D FLAIR,

3D T1w images before and after the injection of gadobutrol 0.1 mg/kg (Gadovist®, Bayer Schering Pharma AG, Berlin, Germany), 2D T2w images, diffusion tensor imaging, DCE-MRI, T_1 relaxometry and DSC-MRI. Sequence parameters are shown in Table 4.

Two different DCE-MRI sequences were used. The T_2* effect on the initial AIF and the effect on the estimated parameters in the first eight patients of the study using a double echo DCE-MRI sequence[91]. This led to two DCE-MRI sequences with T_s of 3.4 s and 2.1 s, a total of 100 and 150 dynamic images and a T_{acq} of 330s and 340s respectively. For details see Table 5.

0.1 mmol/kg of gadobutrol was injected in a right cubital vein using a power injector for both the DCE-MRI and DSC-MRI at a rate of 5 and 3 mL/s respectively. A 20 mL/s saline flush followed to ensure coherence in the passage through the arm.

3.4 Computer simulations

In paper I and II computer simulations were performed using Matlab version MatlabR2011A and MatlabR2013B, (The Mathworks Inc, Natick, MA, US).

Systematic investigation of temporal resolution and total acquisition time through numerical simulations was done in paper I. An AIF was generated by JSim (http://physiome.org/jsim) from the dispersion model developed by Barboriak et al[157]. Tissue response curves were generated from a range of clinical relevant parameters from equation 6. In Paper I the AIF and tissue response curve were downsampled and truncated using the same method as for the clinical data. In Paper II the tissue response curve and the AIF were analyzed using both random $T_1(0)$ between 600 and 2200 ms and a fixed value of 1490 ms (the median value in all tumors).

3.5 Data analysis

All post-processing was done using nordicICE (Nordic NeuroLab AS, Norway) and Matlab R2011A (The MathWorks Inc, Natwick, MA).

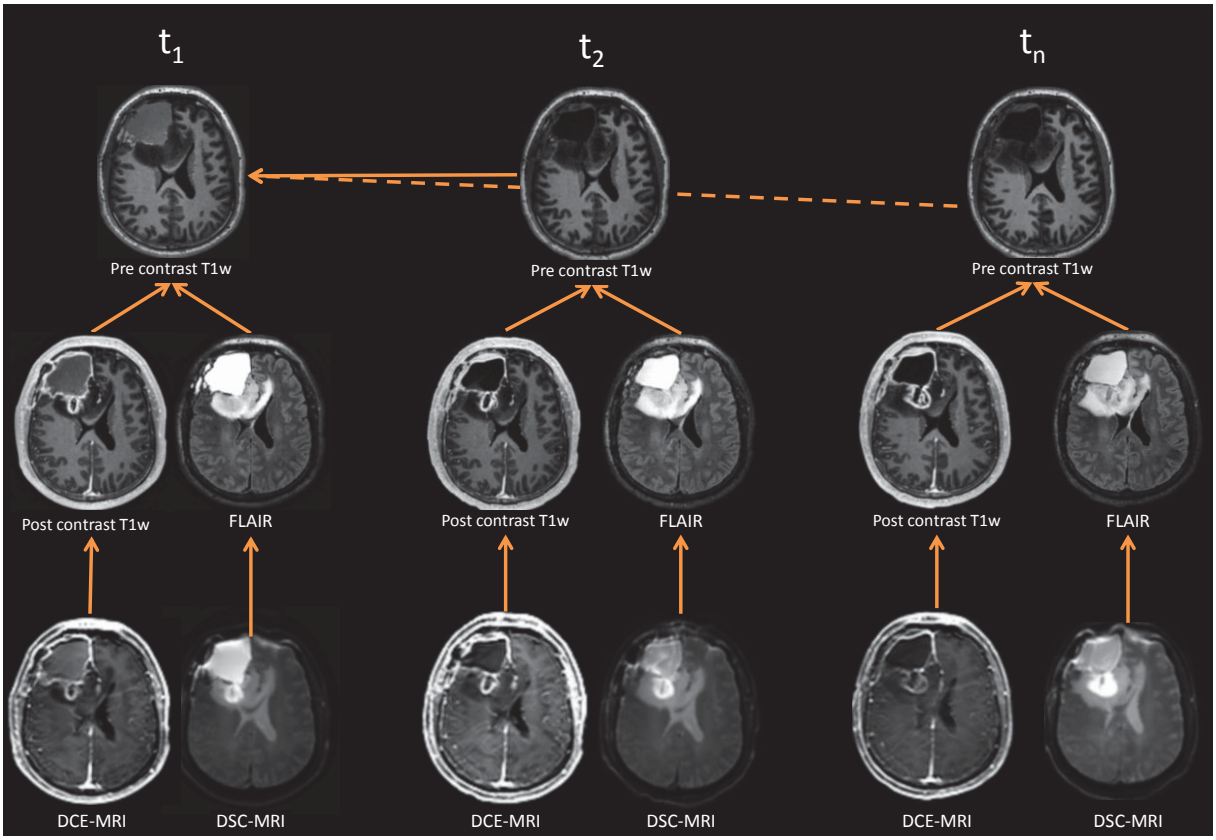

Figure 9: Flow chart of co-registration. First each T1w pre-contrast image at each time point (t) was co-registered to the pre-contrast T1w at baseline (t_1). Then the post-contrast T1w and FLAIR images were co-registered to the transformed pre-contrast T1w images at each time point. Finally motion corrected DCE-MRI and DSC-MRI series were averaged to produce increased image contrast and co-registered to the transformed post-contrast T1w and FLAIR images respectively at each time point. This was repeated for all time points (t_n) (dashed arrow).

3.5.1 Image co-registration

All images were collected in a central database and anonymized using an in-house software, iCat, for removal of all personal information. All structural images were co-registered to the first pre-contrast T1w image series of each patient. Rigid motion correction was performed for the dynamic perfusion images[158]. The dynamic series

were then averaged into one volume and co-registered to the most similar structural images (i.e. DCE-MRI series to post-contrast T1w images and DSC-MRI series to FLAIR images). See figure 9 for details.

3.5.2 Region-of-Interest generation

In paper I and II ROIs were generated using an in-house semi-automatic method for 3D tumor delineation. Skull stripping of the brain was done using the FLAIR images to remove all non-brain tissue[159]. Skull-stripped post-contrast T1w images were then created using FLAIR brain masks as a template. A cluster analysis automatically chose the high-intensity areas in the FLAIR images using a second-order relative entropy thresholding method, creating an automatic generated edema mask ROI for each scan time[160,161]. The edema masks were overlaid on the T1w images and high intensity areas in the T1w images inside the edema masks were then included in a contrast mask. This automatically generated ROI included all hyperintense areas from the post-contrast T1w images. An experienced neuroscientist manually inspected all ROIs and removed non-tumor pixels using an in-house pixel editor creating a mask for the contrast enhancing tumor. Each slice in the DCE-series was then averaged from a dynamic series to a single image stack containing high post-contrast information and co-registered to the tumor mask. The estimated kinetic values in the tumors were then extracted using the ROI on the generated kinetic parameter maps. In paper III, a semi-automatic segmentation was done based upon the method used in Paper I and II[162]. The created edema mask was manually edited to remove non-edema high intensities from the FLAIR images. The manually edited contrast enhancing tumor was then subtracted from the edited edema mask to remove overlapping regions. All ROIs were manually edited if needed and

finally approved by a single MRI radiologist with four years experience. The framework is shown in figure 10.

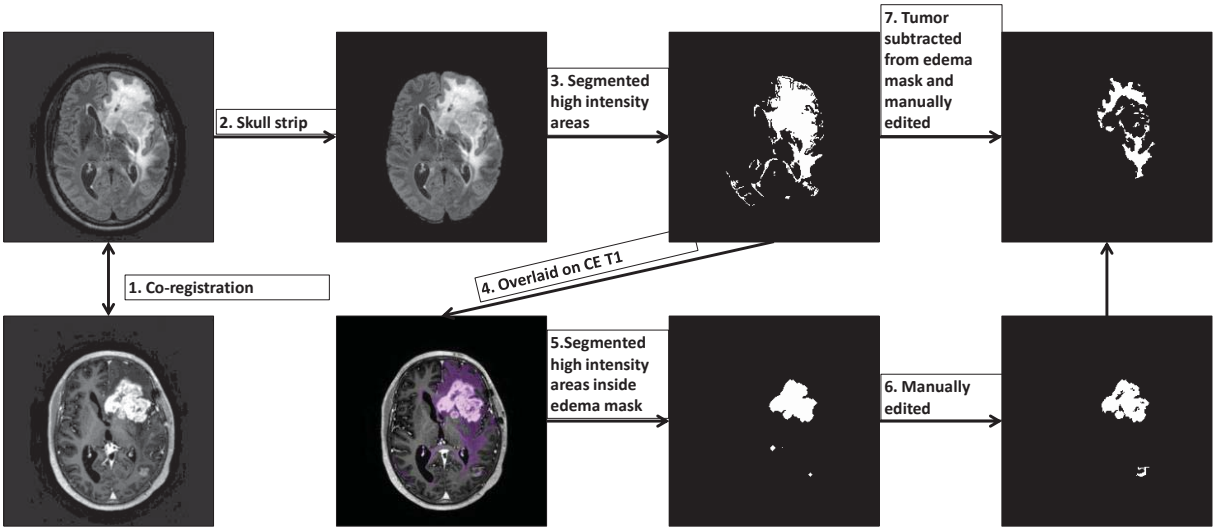

Figure 10: Framework for ROI generation. The numbers represent the chronological order of the process. Step 1-6 was done in all papers and step 7 added for Paper III to create a ROI for non-enhancing tumor in addition to the contrast enhancing tumor from paper I and II.

3.5.3 Downsampling and truncation

In paper I temporal downsampling was done by averaging multiple successive time-points in the dynamic series to give downsampling factors between two and twenty. Each pixel was averaged in a motion corrected series *n* times for a downsampling factor of *n*. As mentioned in Section 3.3. two different DCE-MRI sequences were used. Thus, ten new dynamic series were generated with a T_s between 3.4s and 68s for the first sequence and 2.1s to 42s for the second. Figure 11 a shows the AIF and tissue response function of T_s of 3.4s, 13.6s and 34s. The higher SNR achievable from a dynamic series with low T_s and identical spatial coverage, was thus somewhat accounted for by averaging compared to the selection of individual images. Baseline scans before the arrival of CA were excluded from the averaging process to reduce potential errors from

temporal jittering[83]. Correction of the delay between the AIF and the tissue response function was done with the bolus arrival time method[163].

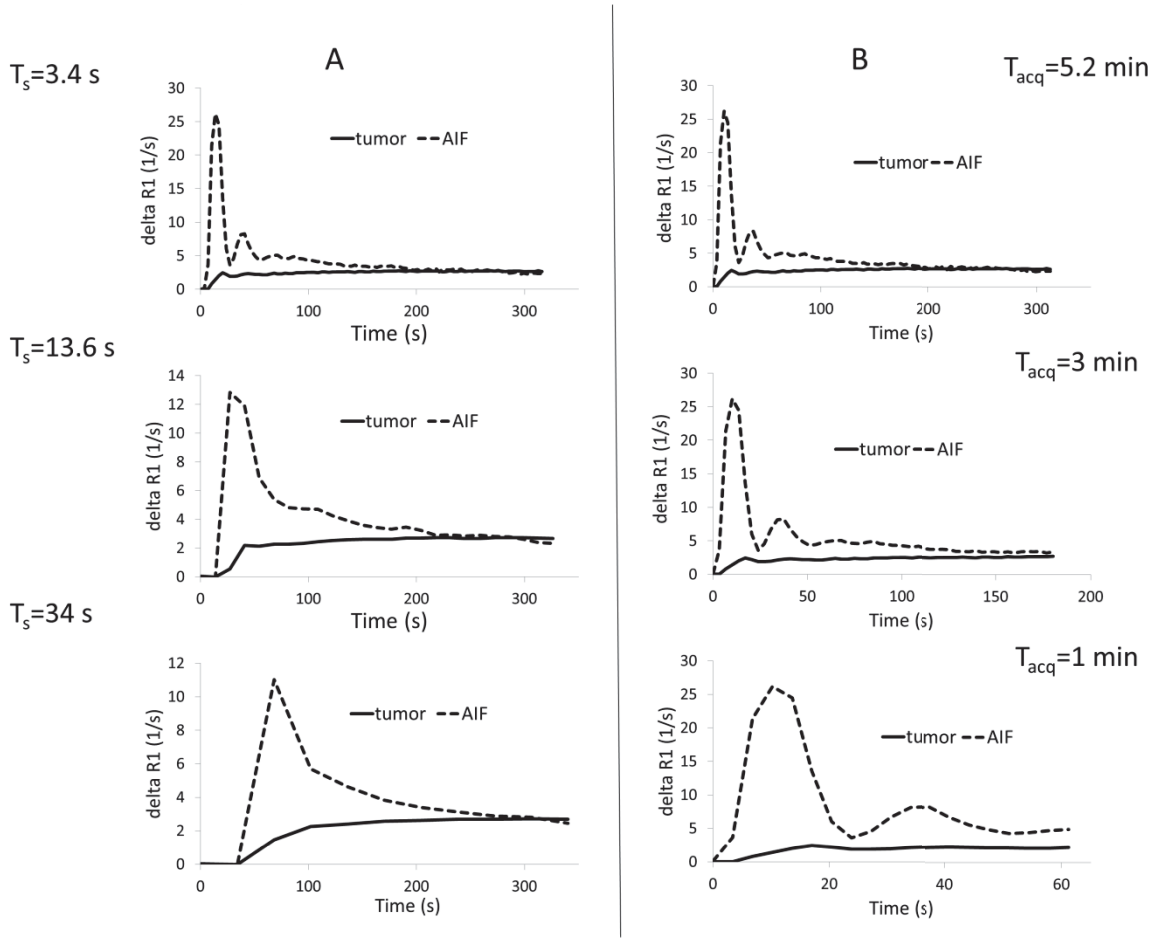

Figure 11: Concentration-time-curves obtained from tumor and arterial input function in a sample patient, showing effects of downsampling (decreasing T_s) (a) and data truncation (reducing T_{acq}) (b) of the original concentration-time-curves. Reproduced with permission from Paper I.

The effect of T_{acq} was investigated by truncating the DCE-MRI time series. The tail of the DCE-series and AIFs were excluded from the analysis by choosing a percentage of the dynamic images series to exclude. Utilizing this truncation option, series with a T_{acq} of 1, 2, 3, 4 and 5 min were used to estimate kinetic parameter maps. A different number of dynamic scans were available in series 1 compared to series 2, due to different T_s. Concentration-time-curves from the truncations in a sample patient can be seen in figure 11 b.

3.5.4 Arterial input generation

A scan-specific AIF was generated for each examination in paper I and II. In paper III a patient-specific AIF from the first exam was used. This has proved to be more robust than scan-specific or population-based AIFs in earlier work looking at double baseline scans in both DCE-MRI and DSC-MRI[89,90]. The AIF was detected semi-automatically with a fixed baseline $T_1(0)$ in blood of 1664 ms[164]. A brain area likely to contain large arteries was manually selected, and an automated AIF detection algorithm averaged the signal from the five best pixels inside the search area[165]. Criteria for a good, clean arterial signal included a high first pass peak, small dispersion of the first pass bolus and a high signal in the tail part of the AIF. The availability of large arteries depended heavily on the tumor location as the imaging stack covered only 44 mm. The middle cerebral artery was selected when inside the imaging stack. In tumors located in the superior aspects of the brain, smaller arteries were chosen. To account for the signal differences depending on the size and direction of the vessel, partial-volume correction was done. A venous output function was detected using the same algorithm as for AIF detection. The search region was placed over the superior sagittal sinus or transversal sinus in the posterior part of the brain. A partial volume correction factor from the estimated ratio of the area under the curve in the AIF and the venous output function was then estimated to scale the AIF. In paper I, the AIFs went through the same regime of averaging to produce AIFs with identical SNR properties and temporal characteristics as the downsampled DCE-series.

3.5.5 Dynamic contrast-enhanced magnetic resonance imaging analysis

The extended Tofts model, described in Section 1.2.3., was used in the analysis of the DCE-MRI data in all papers. Singular value decomposition was used to deconvolve the AIF to the tissue response curve and the estimation of ΔR from the signal intensity. A fixed $T_1(0)$ was used in paper I and III, in paper II both individual $T_1(0)$ maps from Lock-Looker-based relaxometry and the global median $T_1(0)$ in all tumors were used. Voxel-by-voxel analysis yielded estimated kinetic parameter maps of K^{trans}, k_{ep}, v_e and v_p. In paper III CBF was also generated from the DCE data using the same method as was used in DSC-MRI[68].

3.5.6 Dynamic susceptibility contrast magnetic resonance imaging analysis

The DSC-MRI analysis used the established tracer kinetic model described by Østergaard et al[68]. A patient-specific AIF from the first exam was used in all patients and the EPI sequence was corrected for geometric distortions[65]. Parametric maps of CBV and CBF using the patient-specific AIF and rCBV and rCBF were estimated on a voxel-by-voxel basis.

Table 4: Overview of the imaging protocol in the material.

Sequence	Sequence	Geometry(mm)	Matrix	TE/TR(ms)	Slices	Time(s)
FLAIR	3D IR TSE	1.07x1.07x0.6	224x224	424/8000	300	520
T1w	3D GRE - FFE	1.0x1.0x1.0	256x232	2.3/5.1	190	400
T2w	2D SE - TSE	0.45x0.45x2.5	400x255	80/3000	28	210
DTI	2D SE - EPI	2.5x2.5x2.5	96x94	60/9686	50	352
T_1 Look-Locker	3D FFE	1.88x1.88x4	120x109	1.4/2.7	11	168
DCE-MRI	3D FFE	1.88x1.88x4	120x119	2.5/5.1	11	121
CE-T1w	3D FFE	1.0x1.0x1.0	256x232	2.3/5.1	190	400
DSC-MRI	2D SE - EPI	1.88x1.88x4.0	120x118	70/1349	13	112

Abbreviations: TE: time of echo, TR: repetition time, FLAIR: fluid-attenuated inversion recovery, IR: inversion recovery, TSE: turbo spin echo, T1w: T1 weighted imaging, GRE: gradient echo, FFE: fast field echo, T2w: T2 weighted imaging, SE: spin echo, DTI: diffusion tensor imaging, EPI: echo planar imaging, DCE-MRI: dynamic contrast-enhanced magnetic resonance imaging, CE: contrast enhanced, DSC: dynamic susceptibility contrast.

Table 5: Sequence parameters for the two dynamic contrast enhanced magnetic resonance imaging sequences used in the thesis.

	TE(ms)	TR(ms)	FA	TD (ms)	Dynamic scans	T_s (s)	T_{acq} (s)
Sequence 1	2.5	8.2	26	80	100	3.4	330
Sequence 2	2.5	8.2	26	50	150	2.1	340

Abbreviations: TE: echo time, TR: repetition time, FA: flip angle, TD: delay time, T_s: temporal resolution, T_{acq}: total acquisition time.

4 *Summary of papers*

Paper I: Sampling Requirements in DCE-MRI Based Analysis of High Grade Gliomas: Simulations and Clinical Results. J Magn Reson Imaging 2013;37:818-829.

In Paper I we investigated the effect of temporal resolution and total acquisition time on the precision and accuracy in estimated parameters using the extended Tofts model in DCE-MRI to address the lack of studies in large patient materials and clinical settings.

Computer simulations were done to test the theoretical effect of changing T_s and T_{acq} as a function of k_{ep}. DCE-MRI data from 101 examinations in 15 patients were investigated for T_s between 2.1 and 68 s and T_{acq} between 1 min and 5.2 min. The error in the estimated parameters was compared to the sequence with shortest T_s and longest T_{acq}.

The results from the simulations showed an oscillating effect of all parameters for a T_s less than 20 s. At T_s higher than 20 s a reduction in K^{trans}, k_{ep} and v_e as well as an increase in v_p were found. A similar trend was seen in the clinical data for K^{trans} and v_p, significant at T_s < 20s. The effect was more prominent for the highest values of the estimated parameters. From the T_{acq} analysis overestimation of K^{trans} and k_{ep} and underestimation of v_e and v_p were seen increasingly for shorter T_{acq} in both simulations and clinical data.

In conclusion the total acquisition time and sampling time in DCE-MRI influences the precision and accuracy in HGGs. The changes are small in median estimated values of the kinetic parameters at T_s < 20 s. However, the precision is reduced due to larger errors in the highest values. For T_{acq} at least 5 min of scan time is recommended and the error introduced is biased towards regions with low permeability.

Paper II: T_1 in High-Grade Glioma and the Influence of Different Measurement Strategies on Parameter Estimations in DCE-MRI. J Magn Reson Imaging 2015;42:97-104.

Paper II sought to investigate the evolution of $T_1(0)$ in HGG during therapy and the effect of using a fixed value compared to a $T_1(0)$ map on the estimated kinetic parameters in DCE-MRI.

Simulations and clinical data of 196 examinations in 23 HGG patients were assessed. The evolution of the median $T_1(0)$ in tumor trough all examinations was estimated. The percentage error in the estimated kinetic parameters using a fixed $T_1(0)$ value compared to a $T_1(0)$ map was examined both for median tumor values and for the distribution of parameters in the whole tumor.

$T_1(0)$ increased during treatment. The errors introduced by using a fixed $T_1(0)$ value had an inverse relationship with $T_1(0)$ error. Despite this error, a strong correlation was seen between the estimated parameters from both methods when change in median tumor values from one examination to the next was compared. Changes in the histogram normalized peak height were dependent upon the $T_1(0)$ error. If the median $T_1(0)$ in tumor was higher than the fixed value a narrowing of the histogram was seen, resulting in decreased apparent heterogeneity of the tumor. Conversely, if the $T_1(0)$ was lower than the fixed value a broadening of the histogram was seen leading to increased heterogeneity.

Paper II shows that despite changes in $T_1(0)$ during treatment, the ability to assess changes in median tumor values are similar when using a fixed $T_1(0)$ value. The histogram distribution is, however, affected by the introduced $T_1(0)$ error.

Paper III: Prediction of Survival and Progression in Glioblastoma Patients using Temporal Perfusion Changes during Radiochemotherapy. (Submitted)

Radiographic assessment of GBM is based upon the structural RANO Criteria and is not done during the first three months after radiochemotherapy due to difficulties of separating pseudoprogression and tumor recurrence. Early prognostic imaging markers are sought after to accurately predict survival. Paper III explored the evolution of tumor volume and estimated parameters from both DCE-MRI and DSC-MRI during and two weeks past radiochemotherapy. Tumor volume, perfusion and permeability metrics were investigation for early OS prediction.

23 GBM patients were examined by comprehensive MRI before, every second week during and two weeks past radiochemotherapy. CBF, K^{trans} and v_p from DCE-MRI and both absolute and relative CBF and CBV from DSC-MRI were estimated. Temporal evolution and change from baseline were assessed for all parameters. The patients were separated in two groups based upon median OS and the parameter differences between the groups were investigated. Survival analysis was then performed including the creation of a prediction index.

Volume of contrast enhancing tumor and perfusion metrics from DSC-MRI decreased during treatment but no prognostic value was seen between the survival groups. Smaller changes in the DCE-MRI metrics were seen. Patients with an increase in median CBF and K^{trans} from the DCE-MRI analysis larger than 30 % and 10 % compared to baseline had a significantly worse prognosis than the other patients. Multivariate analysis of K^{trans} and rCBV from DSC-MRI revealed an index closely corresponding to OS.

Paper III shows that several changes in structural and functional parameters are evident during radiochemotherapy treatment of GBM patients. For early survival prediction DCE-MRI was more robust than DSC-MRI derived metrics. Combining parameters from several modalities potentially increases the predictive value of early MRI.

5 Discussion

This thesis investigates DCE-MRI of HGG patients during standardized radio-chemotherapy. In Paper I and Paper II we focus on methodological considerations. Paper III investigate the prognostic value of DCE-MRI, through the methods developed in Paper I and II, and compare the results to DSC-MRI and radiologic assessment by structural imaging and the RANO Criteria.

5.1 Temporal resolution and total acquisition time

In Paper I we focus on the temporal requirements in DCE-MRI, both regarding T_s, and T_{aqc}. Previous studies have predominantly been simulation studies investigating errors in the estimated parameters and the results are typically not clearly linked to the clinical relevance in defined patient populations. The results in Paper I indicate that the median value of K^{trans}, k_{ep} and v_e in a tumor ROI is almost independent of T_s for values below 20 s. This is similar to the results from a simulation study be Cheng[84]. However, despite small effects on median tumor values, undersampling resulted in decreased precision of the highest K^{trans} values which may lead to a bias in the estimated values in heterogeneous tumors by underestimation of a (small) fraction of voxels with high K^{trans}. This is clearly seen in figure 12 a. Depending on how tumor K^{trans} and other kinetic parameters are evaluated, i.e. using median tumor value versus hot-spot or histogram distribution, high T_s might be warranted for accurate estimation of the highest K^{trans} values.

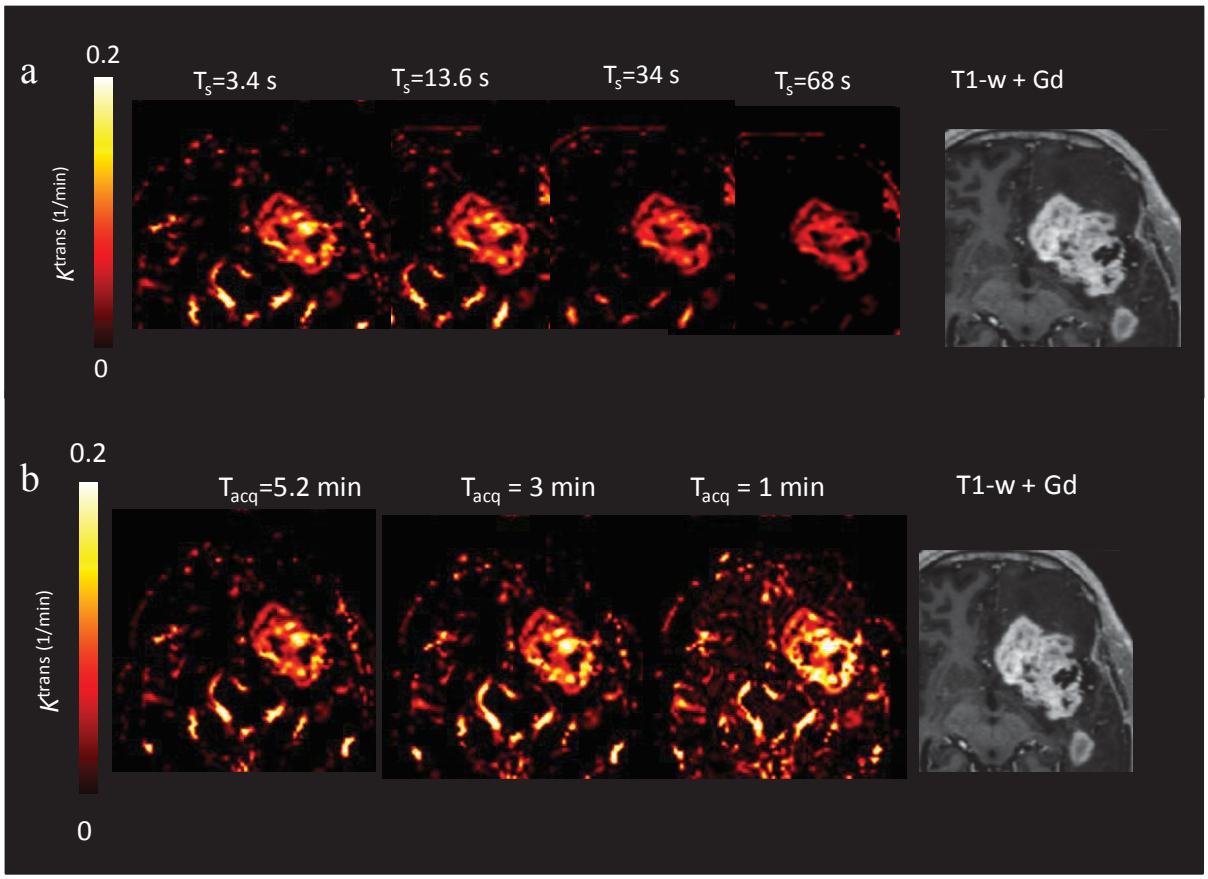

Figure 12: Parametric maps of K^{trans} obtained from a sample patient in Paper I at different T_s showing the effect of temporal downsampling (a). Effect of T_{acq} on estimated parametric K^{trans} maps is shown in (b). Loss of heterogeneity and loss of high K^{trans} values are seen at a T_s of 34 and 68 s and increased high K^{trans} values are seen at a total acquisition time of 3 and 1 minutes. Figure from Paper I and reproduced with permission.

In regards to T_{acq}, a shortening in T_{acq} resulted in overestimation of K^{trans} and k_{ep} and underestimation of v_e and v_p. Reduced total sampling time therefore has the opposite effect to reduced T_s in that the resulting measurement error is biased toward regions with low permeability. This bias leads to a broadening of the tumor histogram distribution by increasing the relative weighting toward higher K^{trans} values, as shown in Figure 12 b. Simulations showed the same tendency and suggested a T_{acq} of at least 6 minutes for accurate estimation of kinetic parameters; however, this would increase the probability of patient motion which could negate the gain from more robust kinetic analysis. In this analysis only the standard Tofts model was used where the K^{trans} reflects

both CBF and PS. In more advanced models trying to separate these parameters higher T_s is required[80].

5.2 T_1 mapping

$T_1(0)$ is needed in DCE-MRI for conversion of signal intensity to change in T_1 as discussed in Section 1.2.3. Haacke et al. found after review of DCE-MRI experiments that noise in the $T_1(0)$ mapping was the single biggest contributor to error in the estimated parameters[94]. They proposed the use of a fixed $T_1(0)$ value and to serially normalize the estimated parameters between imaging time points. This method assumes that $T_1(0)$ stays constant during treatment and was found to yield consistent results. Similarly, Guo et al found that normalized values of K^{trans} and v_e are independent of $T_1(0)$ if there is no change in $T_1(0)$ during treatment. However, the absolute values were heavily dependent on $T_1(0)$[86]. In this study significant change in $T_1(0)$ during therapy was apparent in all patients within a range of 30-366 ms change from the first $T_1(0)$. Using a fixed $T_1(0)$ is therefore dependent on the knowledge of the evolution of $T_1(0)$ during disease progression. In paper II we assessed the change of $T_1(0)$ in HGGs over time and observed a significant increase during treatment, evident after radiochemotherapy at two weeks and three months respectively. This coincides with the recommended first MRI control according to the National Comprehensive Cancer Network[96]. Because of the linear relationship between percentage change in $T_1(0)$ and the normalized ratio of estimated parameters, the effect of using incorrect $T_1(0)$ is dependent on the ground truth value. An error of 100 ms is much larger if the ground truth value is 800 ms compared to 1400, as shown in figure 13. Knowledge of the ground truth values and evolution of $T_1(0)$ during treatment and progression is thus needed if a fixed $T_1(0)$ is used.

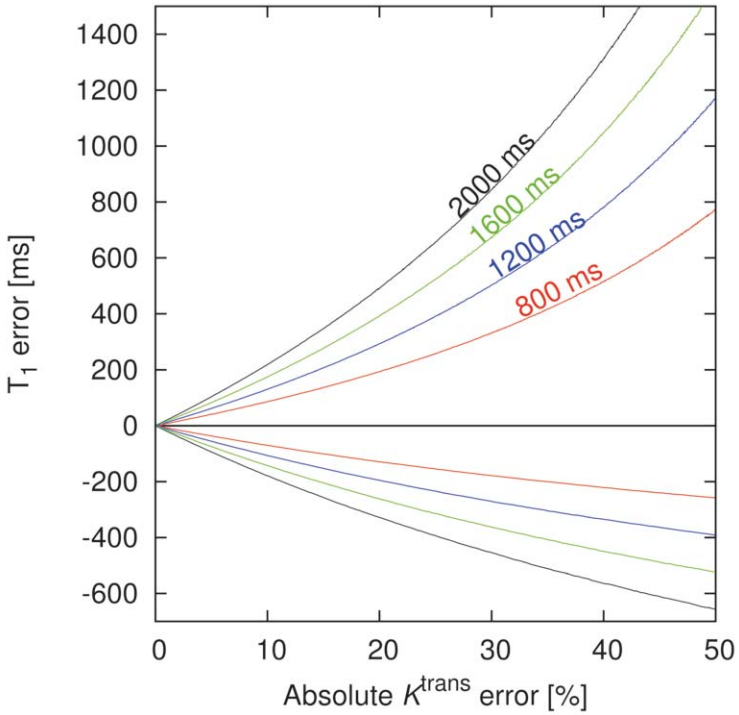

Figure 13: Simulation of resulting error in K^{trans} for a given absolute T_1 deviation from ground truth. A positive T_1 value represents a fixed value higher than the ground truth (overestimation) and a negative value represents a fixed value lower than the ground truth value (underestimation). Ground truth T_1 value displayed above the individual curves. T_1 deviations are better accepted for high ground truth values compared with low and overestimation of the fixed T_1 value is better than underestimation. Reproduced with permission from Paper II.

Paper II found a median $T_1(0)$ in all tumors of 1490 ms. Lower values were seen consistently during radiochemotherapy with an increase two weeks after end of treatment. A fixed $T_1(0)$ value of 1490 ms used in this period would primarily have an effect on the distribution of the estimated parameters. In general, the changes of the median values of K^{trans}, v_p and v_e from one examination to the next were larger than the error introduced by a fixed $T_1(0)$ value. A hot-spot method or histogram analysis, where specific assessment of upper percentile values are required, would be much more susceptible to errors if a fixed $T_1(0)$ value is used. Therefore, the importance of measuring a correct $T_1(0)$ is heavily dependent on the analysis method being applied. This can be amended to some extent by using a higher fixed $T_1(0)$.

5.3 Issues with prognostic imaging markers

An increasing amount of publications of imaging markers are emerging in HGGs, as summarized in Section 1.4. Both structural imaging and pMRI have shown promise as prognostic markers. Widespread clinical use is, however, hindered by some key issues[166]. Prognostication by structural imaging is difficult the first months after radiochemotherapy end because of pseudoprogression. In line with the RANO Criteria, Paper III demonstrated no value from the structural T1w and T2w series for early OS prognostics. This is not surprising, because of the time-points for assessment during and two weeks after radiochemotherapy. An increase in the CE volume from T1w imaging might be due to pseudoprogression, and indeed, the 5 patients with pseudoprogression had longer OS than the median in the cohort (38.8 vs. 19.2 months). Moreover, the number of patients included in the study makes separation of the groups with short and long OS difficult unless large differences in the parameter investigated are evident.

Prognostic markers separating pseudoprogression from recurrent disease and/or predicts OS independent of pseudoprogression are warranted for early assessment. High values of K^{trans} and v_p are associated with both worse OS and recurrent disease in independent studies[120,131]. Similarly, high values of rCBV from DSC-MRI are associated with both recurrent disease and worse OS[167,168]. Unfortunately, overlapping rCBV cutoff values are reported for differentiation of pseudoprogression and recurrence, limiting the use of a single mean value[166]. In addition, the reproducibility in both DSC- and DCE-MRI poses a challenge. To adjust for these issues several approaches are used. The use of serial MRI reduces inter-patient variations and is less sensitive to scanner and site effects. Furthermore, double baseline data has been used to create confidence intervals for the expected within-patient variation of the estimated parameters[169]. Using the

expected patient variation as a baseline increases the confidence that true change is measured. Unfortunately, this demands two MRI examinations and increases study cost.

Dichotomization of parametric values is frequently used for easier interpretation of MRI parameters. This can be done by receiver operating characteristics (ROC) curve analysis and the best cutoff between sensitivity and specificity can be found from the Youden index[170]. As mentioned in Section 1.3.4., a rCBV higher than 1.75 was found to predict shorter PFS in a large patient material[140,171]. This cutoff did not predict OS. In this study, rCBV was measured by manual placement of four ROIs in the areas of highest visible perfusion and the maximum value recorded i.e. the hot-spot method. Emblem et al found significantly higher values for the optimal cutoff between HGG and LGG (3.75-5.58)[116]. In this study both whole tumor histograms and the hot-spot method were examined, with whole tumor histograms proving superior. Moreover, they argue that to obtain the maximum diagnostic accuracy, the choice of optimal cutoff value should be based on data generated at a given site. This is transferable to DCE-MRI and prognostics where different cutoff values are reported, some of them even arbitrarily chosen[131].

The publications in DCE-MRI follow the QIBA recommendations to a large extent. As seen in table 3, research is done on both 1.5 and 3 T scanners. Most studies use a T_s of less than 10 s and a T_{acq} of 4-6 minutes. The main differences between studies are choice of AIF method and reported metrics. In the studies by Ulyte and Bonekamp, the maximum and 90-percentile parametric value of whole tumor histograms were reported[144,154]. The choice of using the 90-percentile value has merit due to the parameter heterogeneity in HGGs and GBMs especially; however maximum values are potentially severely influenced by outliers in noisy data. If maximum value is the preferred metric, a filter removing histogram outliers should be considered. As an

example, the distribution of K^{trans} and rCBV values from our study was investigated (unpublished data), both including all data and by removal of 2% outliers. Outlier removal resulted in a nine-fold reduction in the standard deviation of the maximum value in tumor (Figure 14). The numerical maximum values were also halved when an outlier filter was applied. Outlier removal thus heavily reduces the estimated parameter value and decreases the variability of maximum values.

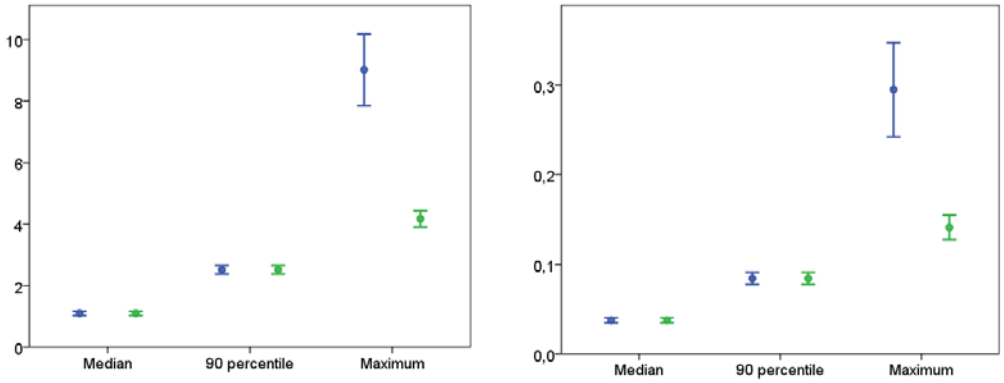

Figure 14: Median, 90-percentile and maximum values of rCBV of the left panel and K^{trans} on the right panel in 240 HGGs. Confidence intervals without the use of a filter shown in blue and confidence intervals after removal of the 2 percent highest values shown in green.

6 Conclusion and future perspectives

6.1 Conclusion

In summary, MRI is an integral part of the assessment of gliomas. Conventional MRI is proven to be suboptimal in the follow-up of tumor evolution, and more advanced methods have been utilized. There is interest in the utility of DCE-MRI to image and quantify BBB disruption in evaluation of disease progression in HGG patients. Despite a standardization of the DCE-MRI model in the late 90´s, a lack of standardization in acquisition method, post-processing and model choice in DCE-MRI is still evident. To address these issues, this thesis focuses on optimization and simplification of DCE-MRI in HGGs in addition to identify optimal perfusion metrics for early OS prognostics. We investigated T_s and T_{acq} requirements and their relations to accurate estimation of parameters in DCE-MRI in Paper I. A T_s of 20 s or less is shown to have small effect on the median value of the estimated parameters except v_p. A T_{acq} of 5-6 min is necessary for accurate parameter estimation. In addition, measurement of $T_1(0)$ is challenging and has been proposed to give rise to uncertainty due to measurement errors. From paper II, we conclude that change in DCE-derived metrics in successive examinations can be measured using a fixed tumor $T_1(0)$ value. This could reduce the total MRI acquisition time by eliminating the need for $T_1(0)$ map generation and make the implementation of DCE-MRI in a clinical setting easier. Further, by repeated MRI during radio-chemotherapy treatment, we find that two weeks past radiochemotherapy end could be a potential optimal time point for early OS assessment from pMRI in GBM. Percentage

change in K^{trans} and CBF from before treatment start is the best predictor for OS in this material.

6.2 Future perspectives

The papers presented in this thesis include a limited number of patients. In Paper III this limits the conclusion on OS prediction. To validate change from baseline as a prognostic marker, a prospective study including a larger sample of patients is needed. Moreover, an investigation of change from baseline in HGG patients from more than one site should be assessed to see if the results from one site are transferable to another.

Furthermore, a standardization of AIF detection method and investigation on how to most accurately measure AIFs in longitudinal studies are warranted. Using double baseline data, different AIF methods can be compared for robustness and preliminary studies have shown that a carry-on AIF from the first examination is more robust than an individual AIF from each exam. In longitudinal studies, despite the tight control of cardiac output and stable overall perfusion to the brain, some changes in the local vascular tumor environment is probable. Thus, the use of a carry-on AIF might be too simplistic.

Lastly, in Paper III a predictive index using K^{trans} and rCBV was found to closely predict OS. This multi-parameter approach warrants further investigation. Although including more than one parameter potentially increases the length of the MRI examination and complexity of the image post-processing, multi-parametric analysis might find patterns of biomarkers that better stratify patients with different response to treatment.

7 *Errata*

The deleted text is marked as ~~strikethrough~~ and the corrections and changes have been marked with **bold**.

Text in the thesis:

Page 12. Line 9. described above ~~above~~ with

Page 20. Line 8. commonly used in DSC-MRI due **to** very

Page 25. Figure 7. Included figure 7 which was lost during pdf conversion.

Page 29. Line 10 and 11. gliomas **are** ~~have a~~ hyperintense ~~signal~~ on T2w imaging and hypointense ~~signal~~ in T1w

Page 31. Line 1. perpendicular ~~of~~ **to**

Page 32. Line 1. RANO criteria ~~points~~ **point** out

Page 45. Line 10. ~~radiotherapy~~ to **radiochemotherapy**

Page 46. Line 1. T1w **images**

Page 46. Line 2. T2w **images**

Page 49. Line 2. ~~Table~~ to **figure**

Page 60. Figure 12 text. ~~Ts~~ to $\mathbf{T_s}$

References. Removal of DOI from reference 29, 49, 57 and 121.

Page 83. Line 7. ~~h?ygradig~~ **høygradig**

Paper III. Page 8. Line 18. Spearman correlation~~)~~.

Paper III. Page 20. Figure 2. Changed figure to color figure mentioned in text.

8 References

1. Goodenberger, M. L. & Jenkins, R. B. Genetics of adult glioma. *Cancer Genet.* **205,** 613–621 (2012).

2. Stupp, R. *et al.* Radiotherapy plus Concomitant and Adjuvant Temozolomide for Glioblastoma. *N. Engl. J. Med.* **352,** 987–96 (2005).

3. Hegi, M. E. *et al. MGMT* Gene Silencing and Benefit from Temozolomide in Glioblastoma. *N. Engl. J. Med.* **352,** 997–1003 (2005).

4. Brandsma, D., Stalpers, L., Taal, W., Sminia, P. & van den Bent, M. J. Clinical features, mechanisms, and management of pseudoprogression in malignant gliomas. *Lancet Oncol.* **9,** 453–461 (2008).

5. Kalpathy-Cramer, J., Gerstner, E. R., Emblem, K. E., Andronesi, O. C. & Rosen, B. Advanced magnetic resonance imaging of the physical processes in human Glioblastoma. *Cancer Res.* **74,** 4622–4637 (2014).

6. Riemenschneider, M. J. & Reifenberger, G. Astrocytic tumors. *Recent Results Cancer Res.* **171,** 3–24 (2009).

7. Louis, D. N. *et al.* The 2007 WHO classification of tumours of the central nervous system. *Acta Neuropathol.* **114,** 97–109 (2007).

8. Kleihues, P. & Ohgaki, H. Primary and secondary glioblastomas: from concept to clinical diagnosis. *Neuro. Oncol.* **1,** 44–51 (1999).

9. Mineo, J.-F. *et al.* Prognosis factors of survival time in patients with glioblastoma multiforme: a multivariate analysis of 340 patients. *Acta Neurochir. (Wien).* **149,** 245–253 (2007).

10. Haldorsen T, E. Cancer in Norway 2009. *Cancer Registery of Norway* 1–98 (2009). Available at: http://www.kreftregisteret.no/en/General/News/Cancer-in-Norway-2009/. (Accessed: 6th October 2013)

11. Louis, D. N. *et al.* The 2016 World Health Organization Classification of Tumors of the Central Nervous System: a summary. *Acta Neuropathol.* **131,** 803–820 (2016).

12. Ohgaki, H. & Kleihues, P. The Definition of Primary and Secondary Glioblastoma. *Clin. Cancer Res.* **19,** (2013).

13. Cohen, A. L., Holmen, S. L. & Colman, H. IDH1 and IDH2 mutations in gliomas. *Curr. Neurol. Neurosci. Rep.* **13,** 345 (2013).

14. Van Den Bent, M. J. *et al.* A clinical perspective on the 2016 WHO brain tumor classification and routine molecular diagnostics. *Neuro. Oncol.* **19,** 614–624 (2017).

15. Reuss, D. E. *et al.* IDH mutant diffuse and anaplastic astrocytomas have similar age at presentation and little difference in survival: a grading problem for WHO. *Acta Neuropathol.* **129,** 867–73 (2015).

16. Olar, A. *et al.* IDH mutation status and role of WHO grade and mitotic index in overall survival in grade II–III diffuse gliomas. *Acta Neuropathol.* **129,** 585–596 (2015).

17. Cairncross, G. *et al.* Phase III trial of chemotherapy plus radiotherapy compared with radiotherapy alone for pure and mixed anaplastic oligodendroglioma: Intergroup Radiation Therapy Oncology Group trial 9402. *J. Clin. Oncol.* **24,** 2707–2714 (2006).

18. Wen, P. Y. & Kesari, S. Malignant Gliomas in Adults. *N. Engl. J. Med.* **359,** 492–507 (2008).

19. Chaichana, K. L. *et al.* Multiple resections for patients with glioblastoma: prolonging survival. *J. Neurosurg.* **118,** 812–20 (2013).

20. Dandy, W. E. Removal of Right Cerebral Hemisphere for Certain Tumors with Hemiplegia. *J. Am. Med. Assoc.* **90,** 823 (1928).

21. Sanai, N., Polley, M.-Y., McDermott, M. W., Parsa, A. T. & Berger, M. S. An extent of resection threshold for newly diagnosed glioblastomas. *J. Neurosurg.* **115,** 3–8

(2011).

22. Simon, M. *et al.* Variant of the Chek2Gene As a Prognostic Markerin Glioblastoma Multiforme. *Neurosurgery* **59,** 1078–1085 (2006).

23. Simpson, J. R. *et al.* Influence of location and extent of surgical resection on survival of patients with glioblastoma multiforme: Results of three consecutive radiation therapy oncology group (RTOG) clinical trials. *Int. J. Radiat. Oncol. Biol. Phys.* **26,** 239–244 (1993).

24. Albert, F. K., Forsting, M., Sartor, K., Adams, H. P. & Kunze, S. Early postoperative magnetic resonance imaging after resection of malignant glioma: objective evaluation of residual tumor and its influence on regrowth and prognosis. *Neurosurgery* **34,** 41–45 (1994).

25. Noorbakhsh, A. *et al.* Gross-total resection outcomes in an elderly population with glioblastoma: a SEER-based analysis. *J. Neurosurg.* **120,** 31–9 (2014).

26. Li, Y. M., Suki, D., Hess, K. & Sawaya, R. The influence of maximum safe resection of glioblastoma on survival in 1229 patients: Can we do better than gross-total resection? *J. Neurosurg.* **124,** 977–988 (2016).

27. Baskar, R., Lee, K. A., Yeo, R. & Yeoh, K.-W. Cancer and radiation therapy: current advances and future directions. *Int. J. Med. Sci.* **9,** 193–9 (2012).

28. Walker, M. D. *et al.* Randomized Comparisons of Radiotherapy and Nitrosoureas for the Treatment of Malignant Glioma after Surgery. *N. Engl. J. Med.* **303,** 1323–1329 (1980).

29. Combs, S. E. in *Gliomas* (ed. von Deimling, A.) 125–140 (Springer Berlin Heidelberg, 2009).

30. Kita, M., Okawa, T., Tanaka, M. & Ikeda, M. [Radiotherapy of malignant glioma--prospective randomized clinical study of whole brain vs local irradiation]. *Gan No Rinsho.* **35,** 1289–94 (1989).

31. Walker, M. D. *et al.* Evaluation of BCNU and/or radiotherapy in the treatment of

anaplastic gliomas. *J. Neurosurg.* **49,** 333–343 (1978).

32. Walker, M. D. *et al.* Evaluation of mithramycin in the treatment of anaplastic gliomas. *J. Neurosurg.* **44,** 655–67 (1976).

33. Walker, M. D., Strike, T. A. & Sheline, G. E. An analysis of dose-effect relationship in the radiotherapy of malignant gliomas. *Int. J. Radiat. Oncol. Biol. Phys.* **5,** 1725–1731 (1979).

34. Hau, E. *et al.* The evolving roles and controversies of radiotherapy in the treatment of glioblastoma. *J. Med. Radiat. Sci.* **63,** 114–123 (2016).

35. Corrie, P. G. Cytotoxic chemotherapy: clinical aspects. *Medicine* **36,** 24–28 (2008).

36. Stewart, L. A. Chemotherapy in adult high-grade glioma: A systematic review and meta-analysis of individual patient data from 12 randomised trials. *Lancet* **359,** 1011–1018 (2002).

37. Taal, W., Bromberg, J. E. & van den Bent, M. J. Chemotherapy in glioma. *CNS Oncol.* **4,** 179–192 (2015).

38. Barbagallo, G. M. V *et al.* Long-term therapy with temozolomide is a feasible option for newly diagnosed glioblastoma: a single-institution experience with as many as 101 temozolomide cycles. *Neurosurg. Focus* **37,** E4 (2014).

39. Helseth, R. *et al.* Overall survival, prognostic factors, and repeated surgery in a consecutive series of 516 patients with glioblastoma multiforme. *Acta Neurol. Scand.* **122,** 159–167 (2010).

40. Combs, S. E., Thilmann, C., Edler, L., Debus, J. & Schulz-Ertner, D. Efficacy of fractionated stereotactic reirradiation in recurrent gliomas: Long-term results in 172 patients treated in a single institution. *J. Clin. Oncol.* **23,** 8863–8869 (2005).

41. Scholtyssek, F. *et al.* Reirradiation in progressive high-grade gliomas: outcome, role of concurrent chemotherapy, prognostic factors and validation of a new prognostic score with an independent patient cohort. *Radiat. Oncol.* **8,** 161 (2013).

42. Weller, M. *et al.* MGMT promoter methylation is a strong prognostic biomarker for benefit from dose-intensified temozolomide rechallenge in progressive Glioblastoma: The DIRECTOR Trial. *Clin. Cancer Res.* **21,** 2057–2064 (2015).

43. Kreisl, T. N. *et al.* Phase II Trial of Single-Agent Bevacizumab Followed by Bevacizumab Plus Irinotecan at Tumor Progression in Recurrent Glioblastoma. *J. Clin. Oncol.* **27,** 740–745 (2009).

44. Friedman, H. S. *et al.* Bevacizumab Alone and in Combination With Irinotecan in Recurrent Glioblastoma. *J. Clin. Oncol.* **27,** 4733–4740 (2009).

45. Khasraw, M., Ameratunga, M. S., Grant, R., Wheeler, H. & Pavlakis, N. Antiangiogenic therapy for high-grade glioma. *Cochrane database Syst. Rev.* **9,** CD008218 (2014).

46. Batchelor, T. T. *et al.* Phase III randomized trial comparing the efficacy of cediranib as monotherapy, and in combination with lomustine, versus lomustine alone in patients with recurrent glioblastoma. *J. Clin. Oncol.* **31,** 3212–3218 (2013).

47. Wick, W. *et al.* Phase III study of enzastaurin compared with lomustine in the treatment of recurrent intracranial glioblastoma. *J. Clin. Oncol.* **28,** 1168–74 (2010).

48. Seystahl, K., Wick, W. & Weller, M. Therapeutic options in recurrent glioblastoma-An update. *Crit. Rev. Oncol. Hematol.* **99,** 389–408 (2016).

49. M. T. Vlaardingerbroek and J. A. den Boer. *Magnetic resonance imaging: theory and practice*. *Springer-Verlag, Berlin* (Springer Berlin Heidelberg, 1996).

50. Brown, R. W., Cheng, Y. C. N., Haacke, E. M., Thompson, M. R. & Venkatesan, R. *Magnetic Resonance Imaging: Physical Properties and Sequence Design*. (Wiley, 2014).

51. Bloch, F. Nuclear induction. *Phys. Rev.* **70,** 460–474 (1946).

52. Purcell, E. M., Torrey, H. C. & Pound, R. V. Resonance absorption by nuclear

magnetic moments in a solid. *Phys. Rev.* **69,** 37–38 (1946).

53. Carr, D. H. *et al.* Gadolinium-DTPA as a contrast agent in MRI: Initial clinical experience in 20 patients. *Am. J. Roentgenol.* **143,** 215–224 (1984).

54. Claussen, C., Laniado, M., Kazner, E., Schörner, W. & Felix, R. Application of contrast agents in CT and MRI (NMR): their potential in imaging of brain tumors. *Neuroradiology* **27,** 164–171 (1985).

55. Kanal, E. Gadolinium based contrast agents (GBCA): Safety overview after 3 decades of clinical experience. *Magn. Reson. Imaging* **34,** 1341–1345 (2016).

56. Wesolowski, J. R. & Kaiser, A. Alternatives to GBCA: Are We There Yet? *Top. Magn. Reson. Imaging* **25,** 171–175 (2016).

57. Roberts, T. P. L. & Noseworthy, M. D. in *Dynamic Contrast-Enhanced Magnetic Resonance Imaging in Oncology* (eds. Jackson, A., Buckley, D. L. & Parker, G. J. M.) 23–37 (Springer Berlin Heidelberg, 2005).

58. Boxerman, J. L., Hamberg, L. M., Rosen, B. R. & Weisskoff, R. M. Mr contrast due to intravascular magnetic susceptibility perturbations. *Magn. Reson. Med.* **34,** 555–566 (1995).

59. FDA Drug Safety. 5-22-2017 FDA Safety Announcement - FDA identifies no harmful effects to date with brain retention of gadolinium-based contrast agents for MRIs: review to continue. *FDA* 2–5 (2017).

60. Tofts, P. S. & Kermode, A. G. Measurement of the blood-brain barrier permeability and leakage space using dynamic MR imaging. 1. Fundamental concepts. *Magn. Reson. Med.* **17,** 357–367 (1991).

61. Maeda, M. *et al.* Tumor vascularity in the brain: evaluation with dynamic susceptibility-contrast MR imaging. *Radiology* **189,** 233–238 (1993).

62. Kono, K. *et al.* The role of diffusion-weighted imaging in patients with brain tumors. *AJNR Am. J. Neuroradiol.* **22,** 1081–1088 (2001).

63. Sinha, S., Bastin, M. E., Whittle, I. R. & Wardlaw, J. M. Diffusion tensor MR imaging of high-grade cerebral gliomas. *Am. J. Neuroradiol.* **23,** 520–527 (2002).

64. Leenders, K. L. *et al.* Cerebral blood flow, blood volume and oxygen utilization: Normal values and effect of age. *Brain* **113,** 27–47 (1990).

65. Vardal, J. *et al.* Correction of b0-distortions in echo-planar-imaging-based perfusion-weighted mri. *J. Magn. Reson. Imaging* **39,** 722–728 (2014).

66. Tamura, H., Hatazawa, J., Toyoshima, H., Shimosegawa, E. & Okudera, T. Detection of deoxygenation-related signal change in acute ischemic stroke patients by T2*-weighted magnetic resonance imaging. *Stroke* **33,** 967–971 (2002).

67. Rother, J., Guckel, F., Neff, W., Schwartz, A. & Hennerici, M. Assessment of regional cerebral blood volume in acute human stroke by use of single-slice dynamic susceptibility contrast-enhanced magnetic resonance imaging. *Stroke.* **27,** 1088–1093 (1996).

68. Østergaard, L., Weisskoff, R. M., Chesler, D. A., Gyldensted, C. & Rosen, B. R. High resolution measurement of cerebral blood flow using intravascular tracer bolus passages. Part I: Mathematical approach and statistical analysis. *Magn. Reson. Med.* **36,** 715–725 (1996).

69. Østergaard, L. *et al.* High resolution measurement of cerebral blood flow using intravascular tracer bolus passages. Part II: Experimental comparison and preliminary results. *Magn. Reson. Med.* **36,** 726–736 (1996).

70. Ellingson, B. M. *et al.* Comparison between intensity normalization techniques for dynamic susceptibility contrast (DSC)-MRI estimates of cerebral blood volume (CBV) in human gliomas. *J. Magn. Reson. Imaging* **35,** 1472–1477 (2012).

71. Bjornerud, A., Sorensen, A. G., Mouridsen, K. & Emblem, K. E. T_1- and T^*_2-Dominant Extravasation Correction in DSC-MRI: Part I—Theoretical Considerations and Implications for Assessment of Tumor Hemodynamic Properties. *J. Cereb. Blood Flow Metab.* **31,** 2041–2053 (2011).

72. Boxerman, J. L., Schmainda, K. M. & Weisskoff, R. M. Relative cerebral blood volume maps corrected for contrast agent extravasation significantly correlate with glioma tumor grade, whereas uncorrected maps do not. *Am. J. Neuroradiol.* **27,** 859–867 (2006).

73. Sourbron, S. P. & Buckley, D. L. Classic models for dynamic contrast-enhanced MRI. *NMR Biomed.* **26,** 1004–1027 (2013).

74. Larsson, H. B. W. *et al.* Quantitation of blood-brain barrier defect by magnetic resonance imaging and gadolinium-DTPA in patients with multiple sclerosis and brain tumors. *Magn. Reson. Med.* **16,** 117–131 (1990).

75. Brix, G. *et al.* Pharmacokinetic parameters in CNS Gd-DTPA enhanced MR imaging. *J. Comput. Assist. Tomogr.* **15,** 621–628 (1991).

76. Tofts, P. S. *et al.* Estimating kinetic parameters from dynamic contrast-enhanced T1- weighted MRI of a diffusable tracer: Standardized quantities and symbols. *J. Magn. Reson. Imaging* **10,** 223–232 (1999).

77. Kety, S. S. The theory and applications of the exchange of inert gas at the lungs and tissues. *Pharmacol. Rev.* **3,** 1–41 (1951).

78. Murase, K. Efficient Method for Calculating Kinetic Parameters Using T 1-Weighted Dynamic Contrast-Enhanced Magnetic Resonance Imaging. *Magn. Reson. Med.* **51,** 858–862 (2004).

79. Kershaw, L. E. & Cheng, H.-L. M. L. M. Temporal resolution and SNR requirements for accurate DCE-MRI data analysis using the AATH model. *Magn. Reson. Med.* **64,** 1772–1780 (2010).

80. Larsson, H. B. W., Courivaud, F., Rostrup, E. & Hansen, A. E. Measurement of brain perfusion, blood volume, and blood-brain barrier permeability, using dynamic contrast-enhanced T_1 -weighted MRI at 3 tesla. *Magn. Reson. Med.* **62,** 1270–1281 (2009).

81. Sourbron, S. P. & Buckley, D. L. On the scope and interpretation of the Tofts

models for DCE-MRI. *Magn. Reson. Med.* **66,** 735–745 (2011).

82. DCE MRI Technical Committee. DCE MRI Quantification Profile, Quantitative imaging Biomarkers Alliance. *Rsna.Org/Qiba* 46 (2012).

83. Henderson, E., Rutt, B. K. & Lee, T. Y. Temporal sampling requirements for the tracer kinetics modeling of breast disease. *Magn. Reson. Imaging* **16,** 1057–1073 (1998).

84. Cheng, H. L. M. Investigation and optimization of parameter accuracy in dynamic contrast-enhanced MRI. *J. Magn. Reson. Imaging* **28,** 736–743 (2008).

85. Parker, G. J. M. *et al.* Experimentally-derived functional form for a population-averaged high-temporal-resolution arterial input function for dynamic contrast-enhanced MRI. *Magn. Reson. Med.* **56,** 993–1000 (2006).

86. Guo, J.-Y., Reddick, W. E., Rosen, M. a & Song, H. K. Dynamic contrast-enhanced magnetic resonance imaging parameters independent of baseline T10 values. *Magn. Reson. Imaging* **27,** 1208–1215 (2009).

87. Yang, C. *et al.* Comparison of quantitative parameters in cervix cancer measured by dynamic contrast-enhanced MRI and CT. *Magn. Reson. Med.* **63,** 1601–1609 (2010).

88. Haroon, H. A. *et al.* A Comparison of Ktrans Measurements Obtained with Conventional and First Pass Pharmacokinetic Models in Human Gliomas. *J. Magn. Reson. Imaging* **19,** 527–536 (2004).

89. Mouridsen, K., Emblem, K. E., Bjørnerud, A., Jennings, D. & Sorensen, A. G. Subject-specific AIF optimizes reproducibility of perfusion parameters in longitudina l DSC-MRI in comparison to session and population level AIF. in *Proc. Intl. Soc. Mag. Reson. Med* (2011).

90. Larsson, C. *et al.* Re-Use of Subject-Specific AIFs Are Warranted in Longitudinal DCE-MRI. in *Proceedings of the ISMRM* **10,** 6408 (2014).

91. Kleppestø, M. *et al.* T2*-correction in dynamic contrast-enhanced MRI from

double-echo acquisitions. *J. Magn. Reson. Imaging* **39,** 1314–1319 (2014).

92. Look, D. C. & Locker, D. R. Time saving in measurement of NMR and EPR relaxation times. *Rev. Sci. Instrum.* **41,** 250–251 (1970).

93. Christensen, K. A., Grant, D. M., Schulman, E. M. & Walling, C. Optimal determination of relaxation times of fourier transform nuclear magnetic resonance. Determination of spin-lattice relaxation times in chemically polarized species. *J. Phys. Chem.* **78,** 1971–1977 (1974).

94. Haacke, E. M. *et al.* New algorithm for quantifying vascular changes in dynamic contrast-enhanced MRI independent of absolute T1 values. *Magn. Reson. Med.* **58,** 463–472 (2007).

95. Cheng, K. *et al.* Rapana thomasiana hemocyanin (RtH): Comparison of the two isoforms, RtH1 and RtH2, at 19 Å and 16 Å resolution. *Micron* **37,** 566–576 (2006).

96. National Comprehensive Cancer Network (NCCN). NCCN Clinical Practice Guidelines in Oncology. *NCCN* 6–12 (2017). Available at: http://www.nccn.org/professionals/physician_gls/f_guidelines.asp. (Accessed: 27th June 2017)

97. Jenkinson, M. D., Du Plessis, D. G., Walker, C. & Smith, T. S. Advanced MRI in the management of adult gliomas. *Br. J. Neurosurg.* **21,** 550–561 (2007).

98. Ellingson, B. M. *et al.* Consensus recommendations for a standardized Brain Tumor Imaging Protocol in clinical trials. *Neuro-Oncology* **17,** 1188–1198 (2015).

99. Upadhyay, N. & Waldman, A. D. Conventional MRI evaluation of gliomas. *Br. J. Radiol.* **84 Spec No,** S107-11 (2011).

100. Pronin, I. N., Holodny, A. I. & Petraikin, A. V. MRI of high-grade glial tumors: Correlation between the degree of contrast enhancement and the volume of surrounding edema. *Neuroradiology* **39,** 348–350 (1997).

101. Asari, S. *et al.* Assessment of the pathological grade of astrocytic gliomas using an MRI score. *Neuroradiology* **36,** 308–310 (1994).

102. Kondziolka, D., Lunsford, L. D. & Martinez, a J. Unreliability of contemporary neurodiagnostic imaging in evaluating suspected adult supratentorial (low-grade) astrocytoma. *J. Neurosurg.* **79,** 533–536 (1993).

103. Möller-Hartmann, W. *et al.* Clinical application of proton magnetic resonance spectroscopy in the diagnosis of intracranial mass lesions. *Neuroradiology* **44,** 371–381 (2002).

104. Macdonald, D. R., Cascino, T. L., Schold, S. C. & Cairncross, J. G. Response criteria for phase II studies of supratentorial malignant glioma. *J. Clin. Oncol.* **8,** 1277–1280 (1990).

105. Therasse, P. *et al.* New Guidelines to Evaluate the Response to Treatment in Solid Tumors. *JNCI J. Natl. Cancer Inst.* **92,** 205–216 (2000).

106. Wen, P. Y. *et al.* Updated response assessment criteria for high-grade gliomas: Response assessment in neuro-oncology working group. *J. Clin. Oncol.* **28,** 1963–1972 (2010).

107. Sorensen, A. G., Batchelor, T. T., Wen, P. Y., Zhang, W.-T. & Jain, R. K. Response criteria for glioma. *Nat. Clin. Pract. Oncol.* **5,** 634–644 (2008).

108. Ruben, J. D. *et al.* Cerebral radiation necrosis: Incidence, outcomes, and risk factors with emphasis on radiation parameters and chemotherapy. *Int. J. Radiat. Oncol. Biol. Phys.* **65,** 499–508 (2006).

109. Brandsma, D. & van den Bent, M. J. Pseudoprogression and pseudoresponse in the treatment of gliomas. *Curr. Opin. Neurol.* **22,** 633–638 (2009).

110. Prager, A. J. *et al.* Diffusion and perfusion MRI to differentiate treatment-related changes including pseudoprogression from recurrent tumors in high-grade gliomas with histopathologic evidence. *AJNR. Am. J. Neuroradiol.* **36,** 877–885 (2015).

111. Kumar, A. J. *et al.* Malignant Gliomas: MR Imaging Spectrum of Radiation Therapy- and Chemotherapy-induced Necrosis of the Brain after Treatment. *Radiology* **217,**

377–384 (2000).

112. Taal, W. *et al.* Incidence of early pseudo-progression in a cohort of malignant glioma patients treated with chemoirradiation with temozolomide. *Cancer* **113,** 405–410 (2008).

113. de Wit, M. C. Y., de Bruin, H. G., Eijkenboom, W., Sillevis Smitt, P. A. E. & van den Bent, M. J. Immediate post-radiotherapy changes in malignant glioma can mimic tumor progression. *Neurology* **63,** 535–537 (2004).

114. Hygino da Cruz, L. C., Rodriguez, I., Domingues, R. C., Gasparetto, E. L. & Sorensen, A. G. Pseudoprogression and Psuedoresponse: Imaging Challenges in the Assessment of Pottreatment Glioma. *American Journal of Neuroradiology* **32,** (2011).

115. Brandes, A. A. *et al.* MGMT promoter methylation status can predict the incidence and outcome of pseudoprogression after concomitant radiochemotherapy in newly diagnosed glioblastoma patients. *J. Clin. Oncol.* **26,** 2192–2197 (2008).

116. Emblem, K. E. *et al.* Glioma grading by using histogram analysis of blood volume heterogeneity from MR-derived cerebral blood volume maps. *Radiology* **247,** 808–817 (2008).

117. Danchaivijitr, N. *et al.* Low-grade gliomas: do changes in rCBV measurements at longitudinal perfusion-weighted MR imaging predict malignant transformation? *Radiology* **247,** 170–178 (2008).

118. Jung, S. C. *et al.* Glioma: Application of histogram analysis of pharmacokinetic parameters from T1-weighted dynamic contrast-enhanced MR imaging to tumor grading. *Am. J. Neuroradiol.* **35,** 1103–1110 (2014).

119. Thomas, A. A. *et al.* Dynamic contrast enhanced T1 MRI perfusion differentiates pseudoprogression from recurrent glioblastoma. *J. Neurooncol.* **125,** 183–190 (2015).

120. Yun, T. J. *et al.* Glioblastoma Treated with Concurrent Radiation Therapy and

Temozolomide Chemotherapy: Differentiation of True Progression from Pseudoprogression with Quantitative Dynamic Contrast-enhanced MR Imaging. *Radiology* **274,** 830–840 (2015).

121. Zhu, X. P., Li, K. L. & Jackson, A. in *Dynamic Contrast-Enhanced Magnetic Resonance Imaging in Oncology* (eds. Jackson, A., Buckley, D. L. & Parker, G. J. M.) 117–143 (Springer Berlin Heidelberg, 2005).

122. Storstein, A. *et al.* Høygradige gliomer hos voksne. *Tidsskr. den Nor. Laegeforening* **131,** 238–241 (2011).

123. Emblem, K. E. *et al.* Predictive modeling in glioma grading from MR perfusion images using support vector machines. *Magn. Reson. Med.* **60,** 945–952 (2008).

124. Sanson, M. *et al.* Isocitrate dehydrogenase 1 codon 132 mutation is an important prognostic biomarker in gliomas. *J. Clin. Oncol.* **27,** 4150–4154 (2009).

125. Lamborn, K. R. Prognostic factors for survival of patients with glioblastoma: Recursive partitioning analysis. *Neuro. Oncol.* **6,** 227–235 (2004).

126. Laws, E. R. *et al.* Survival following surgery and prognostic factors for recently diagnosed malignant glioma: data from the Glioma Outcomes Project. *J. Neurosurg.* **99,** 467–473 (2003).

127. Gerstner, E. R. *et al.* Mgmt methylation is a prognostic biomarker in elderly patients with newly diagnosed glioblastoma. *Neurology* **73,** 1509–1510 (2009).

128. Stupp, R. *et al.* Effects of radiotherapy with concomitant and adjuvant temozolomide versus radiotherapy alone on survival in glioblastoma in a randomised phase III study: 5-year analysis of the EORTC-NCIC trial. *Lancet Oncol.* **10,** 459–466 (2009).

129. Majós, C. *et al.* Early post-operative magnetic resonance imaging in glioblastoma: correlation among radiological findings and overall survival in 60 patients. *Eur. Radiol.* **26,** 1048–1055 (2016).

130. Burth, S. *et al.* Clinical parameters outweigh diffusion- and perfusion-derived MRI

parameters in predicting survival in newly diagnosed glioblastoma. *Neuro. Oncol.* **18,** 1673–1679 (2016).

131. Nguyen, T. B. *et al.* Preoperative prognostic value of dynamic contrast-Enhanced MRI-Derived contrast transfer coefficient and plasma volume in patients with cerebral gliomas. *Am. J. Neuroradiol.* **36,** 63–69 (2015).

132. Kim, S. K. *et al.* The survival significance of a measurable enhancing lesion after completing standard treatment for newly diagnosed glioblastoma. *J. Clin. Neurosci.* **34,** 145–150 (2016).

133. Gzell, C. E., Wheeler, H. R., McCloud, P., Kastelan, M. & Back, M. Small increases in enhancement on MRI may predict survival post radiotherapy in patients with glioblastoma. *J. Neurooncol.* **128,** 67–74 (2016).

134. Li, Y. *et al.* Serial analysis of imaging parameters in patients with newly diagnosed glioblastoma multiforme. *Neuro. Oncol.* **13,** 546–557 (2011).

135. Atkinson, A. J. *et al.* Biomarkers and surrogate endpoints: Preferred definitions and conceptual framework. *Clinical Pharmacology and Therapeutics* **69,** 89–95 (2001).

136. Moffat, B. A. *et al.* Functional diffusion map: A noninvasive MRI biomarker for early stratification of clinical brain tumor response. *Proc. Natl. Acad. Sci.* **102,** 5524–5529 (2005).

137. Hamstra, D. A. *et al.* Functional diffusion map as an early imaging biomarker for high-grade glioma: Correlation with conventional radiologic response and overall survival. *J. Clin. Oncol.* **26,** 3387–3394 (2008).

138. Ellingson, B. M. *et al.* Validation of functional diffusion maps (fDMs) as a biomarker for human glioma cellularity. *J. Magn. Reson. Imaging* **31,** 538–548 (2010).

139. Gerstner, E. R., Sorensen, A. G., Jain, R. K. & Batchelor, T. T. Advances in neuroimaging techniques for the evaluation of tumor growth, vascular

permeability, and angiogenesis in gliomas. *Curr. Opin. Neurol.* **21,** 728–735 (2008).

140. Law, M. *et al.* Gliomas: Predicting Time to Progression or Survival with Cerebral Blood Volume Measurements at Dynamic Susceptibility-weighted Contrast-enhanced Perfusion MR Imaging. *Radiology* **247,** 490–498 (2008).

141. Akgoz, A. *et al.* Spin-echo echo-planar perfusion prior to chemoradiation is a strong independent predictor of progression-free and overall survival in newly diagnosed glioblastoma. *J. Neurooncol.* **119,** 111–119 (2014).

142. Coban, G. *et al.* Prognostic Value of Dynamic Susceptibility Contrast-Enhanced and Diffusion-Weighted MR Imaging in Patients with Glioblastomas. *AJNR. Am. J. Neuroradiol.* **36,** 1247–1252 (2015).

143. Bag, A. K. *et al.* Survival analysis in patients with newly diagnosed primary glioblastoma multiforme using pre- and post-treatment peritumoral perfusion imaging parameters. *J. Neurooncol.* **120,** 361–370 (2014).

144. Bonekamp, D. *et al.* Association of overall survival in patients with newly diagnosed glioblastoma with contrast-enhanced perfusion MRI: Comparison of intraindividually matched T<inf>1</inf>- and T<inf>2</inf>-based bolus techniques. *J. Magn. Reson. Imaging* **42,** 87–96 (2015).

145. Choi, Y. S. *et al.* The Added Prognostic Value of Preoperative Dynamic Contrast-Enhanced MRI Histogram Analysis in Patients with Glioblastoma: Analysis of Overall and Progression-Free Survival. *Am J Neuroradiol* **36,** 2235–2241 (2015).

146. Deike, K. *et al.* Prognostic value of combined visualization of MR diffusion and perfusion maps in glioblastoma. *J. Neurooncol.* **126,** 463–472 (2016).

147. Kim, C. *et al.* Recurrent Glioblastoma: Combination of High Cerebral Blood Flow with MGMT Promoter Methylation Is Associated with Benefit from Low-Dose Temozolomide Rechallenge at First Recurrence. *Radiology* **282,** 212–221 (2017).

148. Sorensen, A. G. *et al.* A 'vascular normalization index' as potential mechanistic biomarker to predict survival after a single dose of cediranib in recurrent

glioblastoma patients. *Cancer Res.* **69,** 5296–5300 (2009).

149. Emblem, K. E. *et al.* Histogram analysis of MR imaging-derived cerebral blood volume maps: Combined glioma grading and identification of low-grade oligodendroglial subtypes. *Am. J. Neuroradiol.* **29,** 1664–1670 (2008).

150. Larsson, C. *et al.* Sampling requirements in DCE-MRI based analysis of high grade gliomas: Simulations and clinical results. *J. Magn. Reson. Imaging* **37,** 818–829 (2013).

151. Zhang, N. *et al.* Correlation of volume transfer coefficient Ktrans with histopathologic grades of gliomas. *J. Magn. Reson. Imaging* **36,** 355–363 (2012).

152. Harrer, J. U. *et al.* Comparative study of methods for determining vascular permeability and blood volume in human gliomas. *J. Magn. Reson. Imaging* **20,** 748–757 (2004).

153. Bisdas, S., Smrdel, U., Bajrovic, F. F. & Surlan-Popovic, K. Assessment of Progression-Free-Survival in Glioblastomas by Intratreatment Dynamic Contrast-Enhanced MRI. *Clin. Neuroradiol.* **26,** 39–45 (2016).

154. Ulyte, A. *et al.* Prognostic value of preoperative dynamic contrast-enhanced MRI perfusion parameters for high-grade glioma patients. *Neuroradiology* **58,** 1197–1208 (2016).

155. Karnofsky, D. A., Abelmann, W. H., Craver, L. F. & Burchenal, J. H. The use of the nitrogen mustards in the palliative treatment of carcinoma. With particular reference to bronchogenic carcinoma. *Cancer* **1,** 634–656 (1948).

156. Association, W. M. World medical association declaration of helsinki: Ethical principles for medical research involving human subjects. *JAMA* **310,** 2191–2194 (2013).

157. Barboriak, D. P., MacFall, J. R., Viglianti, B. L. & Dewhirst, M. W. Comparison of three physiologically-based pharmacokinetic models for the prediction of contrast agent distribution measured by dynamic MR imaging. *J. Magn. Reson. Imaging* **27,**

1388–1398 (2008).

158. Rohde, G. K., Barnett, A. S., Basser, P. J., Marenco, S. & Pierpaoli, C. Comprehensive Approach for Correction of Motion and Distortion in Diffusion-Weighted MRI. *Magn. Reson. Med.* **51,** 103–114 (2004).

159. Smith, S. M. Fast robust automated brain extraction. *Hum. Brain Mapp.* **17,** 143–155 (2002).

160. Studholme, C., Hill, D. L. G. & Hawkse, D. J. An overlap invariant entropy measure of 3D medical image alignment. *Pattern Recognit.* **32,** 71–86 (1999).

161. Chang, C.-I., Du, Y., Wang, J., Guo, S.-M. & Thouin, P. D. Survey and comparative analysis of entropy and relative entropy thresholding techniques. *IEE Proc. - Vision, Image, Signal Process.* **153,** 837 (2006).

162. Odland, A. *et al.* Volumetric glioma quantification: comparison of manual and semi-automatic tumor segmentation for the quantification of tumor growth. *Acta radiol.* **56,** 1396–1403 (2015).

163. Singh, A. *et al.* Improved bolus arrival time and arterial input function estimation for tracer kinetic analysis in DCE-MRI. *J. Magn. Reson. Imaging* **29,** 166–176 (2009).

164. Lu, H., Clingman, C., Golay, X. & Van Zijl, P. C. M. Determining the longitudinal relaxation time (T1) of blood at 3.0 tesla. *Magn. Reson. Med.* **52,** 679–682 (2004).

165. Bjørnerud, A. & Emblem, K. E. A Fully Automated Method for Quantitative Cerebral Hemodynamic Analysis Using DSC–MRI. *J. Cereb. Blood Flow Metab.* **30,** 1066–1078 (2010).

166. Boxerman, J. L. & Ellingson, B. M. Response Assessment and Magnetic Resonance Imaging Issues for Clinical Trials Involving High-Grade Gliomas. *Top. Magn. Reson. Imaging* **24,** 127–136 (2015).

167. Hu, L. S. *et al.* Relative Cerebral Blood Volume Values to Differentiate High-Grade Glioma Recurrence from Posttreatment Radiation Effect: Direct Correlation

between Image-Guided Tissue Histopathology and Localized Dynamic Susceptibility-Weighted Contrast-Enhanced Perfusi…. *Am. J. Neuroradiol.* **30,** (2009).

168. Sugahara, T. *et al.* Posttherapeutic Intraaxial Brain Tumor: The Value of Perfusion-sensitive Contrast-enhanced MR Imaging for Differentiating Tumor Recurrence from Nonneoplastic Contrast-enhancing Tissue. *Am. J. Neuroradiol.* **21,** (2000).

169. Sorensen, A. G. *et al.* Increased survival of glioblastoma patients who respond to antiangiogenic therapy with elevated blood perfusion. *Cancer Res.* **72,** 402–407 (2012).

170. Youden, W. J. Index for rating diagnostic tests. *Cancer* **3,** 32–35 (1950).

171. Law, M. *et al.* Glioma grading: sensitivity, specificity, and predictive values of perfusion MR imaging and proton MR spectroscopic imaging compared with conventional MR imaging. *AJNR Am. J. Neuroradiol.* **24,** 1989–1998 (2003).